

https://dspace.org/

Energy calibration of the 6 MV EN Tandem accelerator of iThemba labs (Gauteng) and measurement of 16O + 16O elastic scattering

Kureba, Chamunorwa Oscar

2011-03-28
http://hdl.handle.net/10539/9247

Downloaded from a DSpace repository. https://dspace.org/

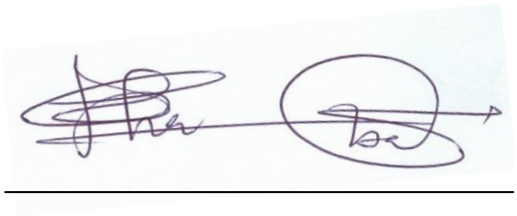
ENERGY CALIBRATION OF THE 6 MV EN TANDEM ACCELERATOR OF iThemba LABS (GAUTENG) AND MEASUREMENT OF $^{16}O + ^{16}O$ ELASTIC SCATTERING

Chamunorwa Oscar Kureba

A Research Report submitted to the Faculty of Science,
University of the Witwatersrand, Johannesburg,
in partial fulfilment of the requirements for the degree of
Master of Science

Johannesburg, 2010

I declare that this research report is my own, unaided work. It is being submitted in partial fulfilment of the requirements for the degree of Master of Science in the University of the Witwatersrand, Johannesburg. It has not been submitted before for any degree or examination in any other University.

Signature: 

Chamunorwa Oscar Kureba

Date: 10th day of August 2010

Abstract

The beam energy stability and reproducibility of the newly refurbished 6 MV EN tandem accelerator of iThemba LABS (Gauteng) (formerly the Schonland Research Institute) has been investigated, followed by an angular distribution measurement of $^{16}O + ^{16}O$ elastic scattering at E_{Lab} = 30 MeV. The 90° beam momentum-analysing magnet system was calibrated using two methods. In one method, the $^{27}Al(p,n)^{27}Si$ reaction was used to determine the proton beam energy from the known neutron emission sharp-threshold of 5.802 ± 0.001 MeV protons. In the other method, the energy of alpha-particles measured at a large backward scattering-angle (θ_{Lab} = 170° ± 2°) from the $^{12}C(^{16}O,\alpha)^{24}Mg^*$ reaction exciting low-lying states in $^{24}Mg^*$ were used to infer the energy of the incident ^{16}O beam. The reaction-product alpha-particle energy was obtained by bracketing with known energies from a thin ^{241}Am α-source. The beam energy measurements were then used to determine the analyser magnet constant. An angular distribution for the elastic scattering of identical particles $^{16}O + ^{16}O$ was measured at a laboratory energy E_{Lab} = 30 MeV, as a test of the calibrated accelerator. The scattering cross-section was measured with the aid of a high resolution ΔE-E gas-ionisation detector. The new elastic-scattering data are consistent with the previously measured values. The optical model theoretical calculation reproduces reasonably well the measured data over the whole angular range as expected.

To Genius Munyati Kureba.

Acknowledgements

Firstly, I would like to thank my supervisor, Prof. J. M. Carter for providing me with the opportunity to embark, at this stage of my life, on studying for a higher degree. His knowledge and wisdom were undoubtedly like a pilot's compass and a soldier's sword to me throughout the duration of my studies.

I greatly appreciate the guidance and insightful comments of my co-supervisor, Prof. E. Sideras-haddad, who also provided me with bursary supplements and a laptop computer, making my studies enjoyable.

I am grateful to iThemba LABS (Gauteng), for financial support and providing the facilities for carrying out this research. I acknowledge also, the University of the Witwatersrand Postgraduate Merit Award for financial support.

Special thanks to the accelerator staff of iThemba LABS (Gauteng), Mr O. Pekar, Mr F. Bulzan and Mr G. Badenhorst, for their skillful driving of the EN tandem accelerator, thus providing the much needed ion beams for the experiments.

I wish to acknowledge with great thanks, the helpful suggestions of my all time friend and fellow academic war veteran, Mr M. Jingo.

I would also like to thank the iThemba LABS (Gauteng) library staff, Ms D. Mahlare and Ms N Radebe, who always offered help and sometimes had to leave their comfort zones to get the references I continuously asked for.

I would especially like to acknowledge the help offered by Dr I Usman, not only in my project data analysis but also during the coursework part of my MSc studies.

Thanks to Dr M Madhuku, for clarifying some concepts in the use of the Origin graphics program and for his endless encouragement.

Of crucial importance also, has been the care and unwavering support of my parents, Mr and Mrs O Kureba. I doubt that I will ever be able to convey my appreciation fully, but I owe them my eternal gratitude. *Vabereki ndinotenda*!

Table of Contents

Contents **Page**

Declaration.....ii

Abstract.....iii

Dedication.....iv

Acknowledgements.....v

List of Figures.....viii

List of tables.....x

Chapter 1 – Introduction.....1

Chapter 2 – Theoretical considerations.....5

2.1 Equations governing an ion beam magnetic analysing system.....5

2.2 Techniques for neutron detection.....7

2.3 Compound nucleus formation and decay.....8

2.3.1 Compound nucleus decay probabilities.....11

2.3.1.1 Particle Decay 12

2.3.1.2 γ-Ray Decay.....12

2.3.1.3 Fission Decay.....12

2.3.2 Resonance reactions.....12

2.4 Optical Model of Elastic Scattering 15

2.4.1 Identical particle scattering.....18

2.5 Δ*E*-*E* Detector.....21

Chapter 3 – Experimental Details, Data analysis and Discussion.....23

3.1 Layout of the Nuclear Physics beam line (C-Line).....23

3.2 Refurbished Accelerator inflection magnet scan.....25

3.3 EN Tandem Accelerator Analyser Magnet Calibration 27

3.3.1 Method 1: $^{27}Al(p,n)^{27}Si$ reaction.....29

3.3.1.1 Eberline BF_3 Neutron Rem Detector.....30

3.3.1.2 Eberline Model ESP-1 Neutron Counter.....31

3.3.1.3 Data analysis.....32

3.3.2 Method 2: $^{12}C(^{16}O,\alpha)^{24}Mg^*$ reaction…….…….....36
3.3.2.1 Data Analysis….....36
3.3.3 Combination of the two calibration methods…….....40
3.4 Measurement of $^{16}O(^{16}O, ^{16}O)\,^{16}O$ identical particle scattering and check against previous results….....…….....42
3.4.1 Use of the Δ*E*-*E* gas-ionisation detector..…….....42
3.4.2 Description of electronics set-up….....…….....44
3.4.3 Data extraction...…….....46
3.4.4 Determination of scattering cross-sections.....…….....48
3.4.5 Optical Model prediction for $^{16}O + ^{16}O$ elastic scattering.....50
3.4.6 Discussion.....…….....52

Chapter 4 – Conclusions.....54

Bibliography 55

Appendix 58

List of Figures

Figure 2.1 Processes in heavy-ion scattering depend on the impact parameter, when energies are large enough to penetrate the Coulomb barrier [KR88]...……...…...9

Figure 2.2 An illustration of fission decay of a compound nucleus ……..13

Figure 2.3 (a) Far from resonance, the exterior and interior wave-functions match badly, and little penetration of the nucleus occurs. (b) As the match improves, there is a higher probability to penetrate. (c) At resonance the amplitudes match exactly, the incident particle penetrates easily, and the cross-section rises to a maximum [KR88] ……..14

Figure 2.4 Identical particle scattering resulting in two indistinguishable events….20

Figure 3.1 Plan view of the C-Line at the 6 MV EN tandem accelerator laboratory of iThemba LABS (Gauteng)……..24

Figure 3.2 *Upper:* Log plot of ion source species identified, using a graphite target in an 860C negative sputter ion-source with source extraction voltage (*V*ext = 23.5 keV). *Lower*: Linear plot of ion source species identified.…….28

Figure 3.3 Part of the C-line experimental set-up to measure neutron yield from the ^{27}Al(p,n)^{27}Si reaction……...……...30

Figure 3.4 Photograph of the Eberline Neutron Rem Detector which was used to detect neutrons in the ^{27}Al(p,n)^{27}Si reaction…….31

Figure 3.5 Photograph of the Eberline Smart Portable (ESP1) neutron counter which was used in the ^{27}Al(p,n)^{27}Si reaction……...32

Figure 3.6 Normalised neutron yield for the ^{27}Al(p,n)^{27}Si reaction, plotted as a function of NMR frequency. The constant

background is shown by the solid line with the upper and lower limits indicated by the dashed lines....…….....34

Figure 3.7 Threshold curve for the $^{27}Al(p,n)^{27}Si$ reaction, showing $(Y\text{-}B)^{2/3}$, where Y is the neutron yield and B is the mean background, plotted as a function of NMR frequency. The error bar on the $^{27}Al(p,n)^{27}Si$ measurement is determined by the upper and lower limits of background subtraction (see Fig. 3.6).....35

Figure 3.8 Energy levels of ^{24}Mg [EN90]……..37

Figure 3.9 Measured energy spectrum from the $^{12}C(^{16}O,\alpha)^{24}Mg^*$ reaction 38

Figure 3.10 *Upper*: Main peaks from an ^{241}Am α-source. *Lower*: Enlarged view of the alpha group for the $^{24}Mg^*$ level at 1.369 MeV of excitation. Gaussian curve fittings are shown around each peak.....39

Figure 3.11 Schematic diagram of the Δ*E*-*E* gas-ionisation detector……...44

Figure 3.12 Electronics block diagram showing the components used in detected signal processing…….....45

Figure 3.13 *Upper*: Two-dimentional Δ*E versus* E_{Total} spectrum of $^{16}O + SiO_2$. *Lower*: Projected one-dimensional spectrum at E_{Lab} = 30 MeV and θ_{Lab} = 23°……..……..47

Figure 3.14 Angular distribution for the elastic scattering of ^{16}O from ^{16}O at E_{Lab} = 30 MeV. The solid curves show *Upper*: the symmetrised ratio-to-Mott optical model calculations using the parameters shown in Table 3.4. *Lower*: symmetrised optical model prediction…….....51

List of Tables

Table 3.1 Analyser magnet calibration constant measurements.....41

Table 3.2 Overview of the data measured in $^{16}O(^{16}O,^{16}O)^{16}O$ reaction…….....42

Table 3.3 Optimum operating conditions for the Δ*E*-*E* gas-ionisation detector….……..……...43

Table 3.4 Optical model potential parameters [CA81] for $^{16}O(^{16}O,^{16}O)^{16}O$…..….....52

CHAPTER 1

Introduction

Only a few accelerators are equipped with absolute systems for measuring the beam energy, therefore, nuclear reaction experiments are performed with energy analysers that require calibration. A calibrated momentum-analysing magnet system determines the absolute energy of an ion beam from an accelerator. Detailed field or beam measurements must be carried out in order to accomplish the required magnet calibration. In principle, field dependent saturation effects are known to be important. As such, measurements over the full range of magnet excitation should be carried out to obtain an accurate calibration. Saturation gives a magnet constant which is a function of magnet excitation [OL87]. In material analysis experiments a highly-defined beam energy is necessary. For example this energy is directly related to the depth profiling and depth resolution in the investigated sample for resonance reactions. Nuclear scattering experiments require the energy of the incident beam to be known as accurately as possible and at least to within about 20 keV in order to determine possible resonance energies. An additional requirement is the quick change of energy without changing the stability conditions.

A refurbishment project of the 6 MV EN tandem accelerator facility of iThemba LABS (Gauteng), formerly the Schonland Research Centre for Nuclear Sciences took two and a half years to complete, starting early in 2005. The initial phase of the project drew to a close with the first beam on target produced on 31 May 2007. The official opening of the new iThemba LABS (Gauteng) EN tandem accelerator facility took place on 2 July 2007, the event of which coincided with the official opening of the 2007 South African Institute of Physics (SAIP) Annual Conference, which was held at the University of the Witwatersrand. The facility had been transferred from Wits to the National Research Foundation (NRF) on 1 January 2005. Since then many improvements to the accelerator have been made: Scanner Beam Profile Monitor (BPM) control and display software, which runs

on the Experimental Physics and Industrial Control System (EPICS), was developed to display beam profiles on a computer screen instead of an oscilloscope; a multiplexer system was developed to automatically select, measure and display the beam current on a Faraday cup on a screen at the control desk; automatically isolating valves for fore-pumps were installed to limit back-streaming of oil under certain operating conditions, especially at the ion source and accelerator tubes; x-ray monitors alongside the accelerator tank monitor X-ray activity, and are also used as a diagnostic tool during accelerator tube conditioning, since X-ray activity provides an early warning of imminent sparking in the tubes as the terminal voltage increases; the old accelerator tubes were replaced with new ones and the original charging belt system was replaced with two pelletron chains [IT08].

The obvious intended outcome of the refurbishment exercise was to achieve the most stable beam possible, given that the refurbished accelerator is required for Accelerator Mass Spectrometry (AMS) with the experimental results having to be competitive with the best in the world, since the facility will be used for both fundamental research and for commercial purposes. The latter also takes into consideration immense interest that had been expressed by industry in the AMS facility, which will be the only one on the entire African continent.

The newly upgraded 860C sputter ion source with a graphite target was used to carry out an inflection magnet scan, as a test of the system and to ascertain which ion beams could be produced from the ion source and injected into the accelerator. The iThemba LABS (Gauteng) 6 MV EN tandem accelerator momentum-analysing magnet bends the beam through 90°. Two different nuclear reactions were then used to determine accelerated ion energies, in order to calibrate the momentum-analysing magnet of the system. In the first method, the $^{27}Al(p,n)^{27}Si$ resonance reaction was used to determine the proton beam energy from the known neutron emission threshold of 5.802 ± 0.001 MeV [OV69]. For the second method, alpha-particle energies from the $^{12}C(^{16}O,\alpha)^{24}Mg^*$ compound nucleus reaction exciting low-lying states in $^{24}Mg^*$ were used to infer the energy

of the incident ^{16}O beam. The reaction-product alpha-particle energy was obtained by bracketing with known energies from a thin ^{241}Am α-source [OL87]. The beam energy measurements in the two reactions were then used to determine a value for the analyser magnet constant.

The Nuclear Physics beam line (C-Line) was completely rebuilt in the refurbishment exercise. Beam-line alignment involved the use of a theodolite and graticles on the beam line components, with the optical line being defined by the tandem analysing magnet. New vacuum pumps have also been incorporated into the line and scattering chambers. Another test of the system was an investigation to determine the characteristics of the high-resolution Δ*E*-*E* gas-ionisation detector which would later be used for nuclear particle identification. Having changed over the gas used in the ionisation chamber from an argon/methane mixture to iso-butane, there was a need to obtain new detector operating parameters [JI09]. Detector electronics and the multi-parameter data acquisition system were also brought back into operation.

Beam energy calibration results were then used to set up the accelerator, which was in turn used in a didactic exercise, checking reliability of the systems through the measurement of an elastic scattering cross-section. An angular distribution for identical particle $^{16}O(^{16}O,^{16}O)^{16}O$ elastic scattering was measured at E_{Lab} = 30 MeV, for which data already existed for comparison [CA81]. The Nuclear Physics beam line (C-Line) was used, where the ^{16}O beam was focused into the small scattering chamber, bombarding a SiO_2 target. A high resolution Δ*E*-*E* gas-ionisation detector with iso-butane gas was used to detect the scattered particles. The CAMAC data acquisition system was used to identify the particles online. Elastic scattering data were fitted with an optical model prediction using known Woods-Saxon optical parameters [BR61, CA81].

This research report is compiled as follows:

- Chapter 2 describes the theoretical considerations and models used for data analysis.

- Chapter 3 describes the experimental details, data analysis and discussion.
- Overall conclusions on the research project are given in chapter 4.
- Appendices, with tabulated measured results are found at the back of the research report.

CHAPTER 2

Theoretical Considerations

A calibrated momentum-analyzing magnet system determines the absolute energy of an ion beam from an accelerator. Nuclear scattering experiments require the energy of the incident beam to be known to within about 20 keV in order to determine possible resonance energies. The theory behind the two calibration reactions, ^{27}Al(p,n)^{27}Si and ^{12}C(^{16}O,α)^{24}Mg* together with the ^{16}O(^{16}O,^{16}O)^{16}O identical particle scattering reaction is described in this chapter.

2.1 Equations governing an ion-beam magnetic analysing system

The beam analysing system of a charged particle accelerator operates on the principle that a charged particle in motion is deflected by a magnetic force and the angle through which the particle is deflected varies with the mass, the energy and the charge of the particle. The governing equation [AN07], given in appropriate units, is

$$B\rho = 144\sqrt{\frac{ME}{z^2}} \ , \qquad (2.1)$$

where $B\rho$ is the magnetic rigidity (kGcm), B is the magnetic field (kG), ρ is the radius of curvature (cm), M is the particle mass (u), E is the beam kinetic energy (MeV), and ($q = ze$) is the particle electric charge.

Magnetic rigidity is defined as a measure of the momentum of a charged particle moving perpendicular to a magnetic field, equal to the magnetic induction times the particle's radius of curvature. It is a quantity of great importance in Accelerator Physics. For a single-stage Van Der Graaf accelerator of conventional design and singly-ionised particles, the E in Eq. (2.1) is equal to the terminal potential V. For a two-stage (tandem) Van der Graaf accelerator and a

singly-charged negative ion injected, the product *ME* in Eq. (2.1) is substituted by the expression:

$$MV(Z+1),$$

where *M* is the mass number of the ion, *V* is the terminal potential and *Z* is the number of charges removed from the neutral atom in the terminal stripper. Using this expression assumes that a singly-charged negative ion is produced in the ion source.

In the ^{27}Al(p,n)^{27}Si and ^{12}C(^{16}O,α)^{24}Mg* analyser magnet calibration reactions, the central field of the magnet is assumed to be proportional to the analyser magnet Nuclear-Magnetic-Resonance (NMR) frequency, as read from an NMR proton-rich probe placed near the midpoint of the beam trajectory within the analyser magnet. The spin angular momentum of the proton can take only two values when placed in a magnetic field, viz, spin up (parallel to the field) and spin down (antiparallel to the field). The energy of the nucleus splits into two levels when a magnetic field is present. The spin up state will have the lower energy while the spin down will have the upper energy. The energy difference between these two levels is proportional to the total magnetic field at the nucleus [GI95]. Energy absorption occurs at resonance, leading to a measurement of magnetic field. The resonance frequency is given by

$$hf_0 = \Delta E = \mu_N g_N B_0, \tag{2.2}$$

where h is Plank's constant, f_0 is the resonance frequency, ΔE is the energy difference between spin states, μ_N is the nuclear magneton, g_N is the nuclear g-factor and B_0 is the magnetic field. From Eq. (2.2), it can be noted that an increase (or decrease) in frequency results in a direct increase (or decrease) in magnetic field, thus, setting the frequency sets the magnetic field.

The analyser magnet calibration factor, *K*, can be determined from the proton threshold frequency, *f* (MHz), using the following expression:

$$K = \left\{ \frac{ME}{Q^2 f^2} \right\} \left\{ 1 + \frac{E}{2Mc^2} \right\}, \tag{2.3}$$

where M is the ion mass (u), which is obtained by subtracting the mass of the appropriate number of electrons from the atomic mass, and neglecting the electron binding energies, E is the particle energy (keV), Q is the particle charge state (e) and Mc^2 is the rest energy (keV) [OV69].

In [OV69] the beam optical elements were designed for ion beams with magnetic rigidities equivalent to that for 175 MeV protons. In [OL87] the magnet was designed for a maximum mass-energy product of 320 MeV amu. However, the 6 MV EN tandem accelerator of iThemba LABS (Gauteng) has a limited range of equivalent proton energies, E_p (0 MeV $\lesssim E_p \lesssim$ 20 MeV), due to the fairly low terminal voltage compared to the ones discussed in [OV69, OL87]. We can, therefore, assume that the value of K is constant.

2.2 Techniques for neutron detection

Due to the fact that neutrons have no charge and, therefore, do not interact directly with the electrons in matter as gamma rays do, mechanisms for detecting neutrons in matter are based on indirect methods, through nuclear reactions that create charged particles. The process of neutron detection begins when neutrons, interacting with various nuclei, initiate the release of one or more charged particles. The electrical signals produced by the charged particles can then be processed by the detection system. Gas-filled thermal-neutron detectors use either ^{3}He or BF_3. In the case of BF_3, the counter is about 96% ^{10}B-enriched and the nuclear reaction that takes place is

$$n + {}^{10}B \rightarrow \alpha + {}^{7}Li^* + 2310 \text{ keV}, \tag{2.4a}$$

$$^{7}Li^* \rightarrow {}^{7}Li + 480 \text{ keV}. \tag{2.4b}$$

This reaction is exothermic and releases energetic charged particles into the gas.

The charged α-particles created in the nuclear reaction ionise the gas. The counters are operated in the proportional mode, and the ionisation produced by these particles initiates the multiplication process that leads to detection. The amount of energy deposited in the detector is the energy available from the nuclear reaction. Because of the large cross-section of the $^{10}B(n,\alpha)$ reaction, the bare (without moderator) BF_3 counter has a high sensitivity for slow neutrons. When the detector is covered with a suitable moderating medium, it makes a sensitive detector for fast neutrons. The BF_3 proportional counter may operate without or with a moderator.

Examples of moderators include polyethylene, paraffin or materials with hydrogen content. The function of the moderator is to present a large scattering cross-section to the neutrons. Through elastic scattering collisions with the moderator nuclei, the fast and epithermal neutrons give up a large part of their energy (a maximum for identical mass scattering, i.e. hydrogen nuclei of the moderator) and are slowed down and ultimately become thermalised. Due to the moderation by the detector housing, the thermal neutron flux densities are attenuated as a result of the high-absorption of the ^{10}B. The detector has a centre anode wire maintained at a high positive potential (~2 kV) with respect to the shell. Boron-trifluoride gas is contained within the shell and the ionisation event causes a burst of electrons to arrive at the anode.

Proportional "long counters" can also be used to detect neutrons. A long counter is just a proportional counter, similar to the one that was used in the $^{27}Al(p,n)^{27}Si$ calibration experiment, but with a specifically designed moderator so that its response is largely independent of the incident neutron energy.

2.3 Compound nucleus formation and decay

Encounters of nucleons or other strongly interacting nuclear beam particles with target nuclei produce a variety of nuclear reactions, depending upon impact parameter, *b* as shown in Fig. 2.1, whose diversity is due to the individual

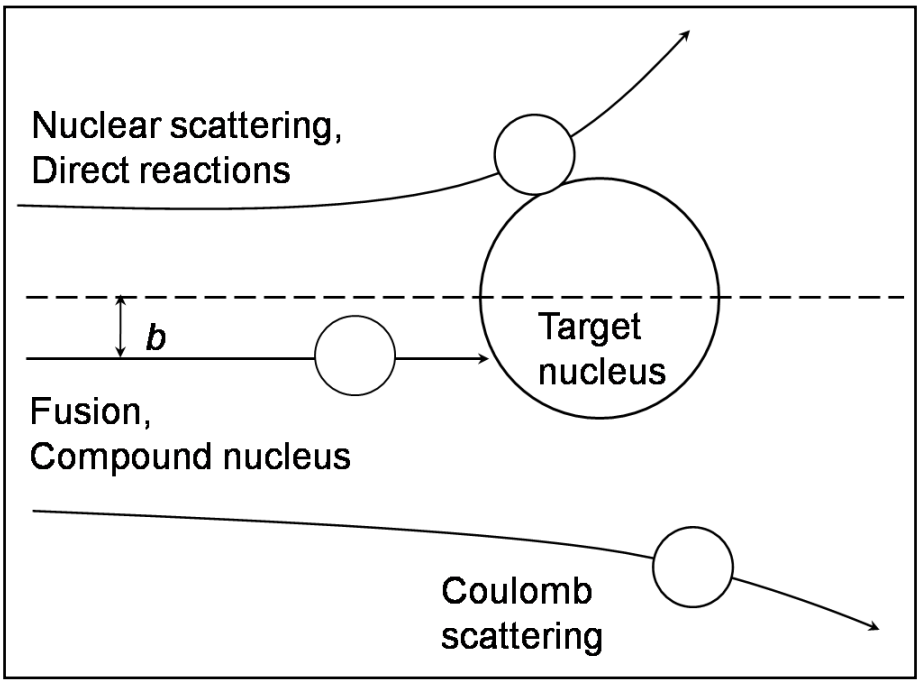


Figure 2.1 Processes in heavy-ion scattering depend on the impact parameter, when energies are large enough to penetrate the Coulomb barrier [KR88].

properties and relative kinetic energies of colliding particles and nuclei. The composition of reaction products depends on the particles and nuclei involved, while their kinematic characteristics are governed by the reaction mechanism [SI90]. In spite of being rather varied, nuclear reactions are conveniently divided into two large groups, i.e. direct reactions and compound nucleus reactions.

Compound nucleus reactions are reactions which proceed via an equilibrated intermediate fused system. Symbolically, the formation and decay of an excited compound nucleus C^* may be written as,

$$a + A \rightarrow C^* \rightarrow b + B, \tag{2.5}$$

where a is the incident particle (projectile), A is the target nucleus, b is the light emitted particle (n, p, d, t, ^{3}He, α) and B is the product (recoil) nucleus which may or may not be excited.

The excitation energy of the compound nucleus is the sum of the centre-of-mass kinetic energy and the Q-value of the reaction. Q-value is defined as the difference between the sum of the rest mass energies of the initial participants of a nuclear reaction and the sum of the rest mass energies of all the products of the reaction. When an incident projectile enters a target nucleus with an impact parameter *b* small compared with the nuclear radius (see Fig. 2.1) there is a high probability of it interacting with one of the nucleons of the target.

In a semi-classical picture, the recoiling nucleon and the incident particle (now with less energy) can each make successive collisions with other nucleons, and after many such interactions, the incident kinetic energy of the projectile is shared among many of the nucleons of the combined system of projectile plus target. Eventually, the average increase in energy of any single nucleon is not enough to free it from the nucleus. However, within the statistical distribution of energies there is a small probability that a single nucleon will gain enough energy to escape.

The relative probability for decay into any specific set of final products is independent of the means of formation, that is, a compound nucleus forgets its means of formation and decays primarily by statistical rules. This is called the independence hypothesis. The independence hypothesis implies that the cross-section for a particular process $\alpha \rightarrow \beta$ can be factorised into the cross-section $\sigma_c(\alpha)$ for the formation of the compound nucleus through the entrance channel α, and the probability that the compound nucleus decays through channel β. Thus

$$\sigma_{\beta\alpha} = \sigma_{\mathrm{cn}}(\alpha)\frac{\Gamma_\beta}{\Gamma}, \tag{2.6a}$$

where Γ_β is the partial width for decay through channel β and Γ is the total width given by

$$\Gamma = \sum_\beta \Gamma_\beta . \tag{2.6b}$$

The compound nucleus model works best for low incident energies (typically

10 - 20 MeV) and medium-heavy nuclei. Nucleons and clusters up to α-particles emitted from the compound nucleus produce a nearly isotropic angular distribution due to the random nature of the decay. As the energy of the compound nucleus increases, more and more particles are evaporated. Below the particle threshold the compound nucleus de-excites by γ-emission [JA70]. The probability of a preformed cluster with mass greater than that of an α-particle, e.g. ^{6}Li, ^{9}Be is very low and, therefore, the yield in compound nucleus decay is negligibly small.

2.3.1 Compound nucleus decay probabilities

A compound nucleus once formed with a given excitation energy, angular momentum and parity decays in a way that is completely determined by the weights of the various possible final states. For the sake of completeness the various mechanisms of compound nucleus decay are described in this section.

2.3.1.1 Particle decay

The rate for emitting a given particle *x* from an excited nucleus 1 to form a product nucleus 2 is determined from [PU77]

$$R_x d\varepsilon_x = \frac{1}{\hbar}\Gamma_x(\varepsilon_x) = \frac{1}{2\pi\hbar}\frac{\rho_2(E_2,J_2,\pi_2)}{\rho_1(E_1,J_1,\pi_1)}\sum_{S=|J_1-S_x|}^{J_1+S_x}\sum_{\ell=|J_1-S_1|} T_\ell^x(\varepsilon_x)d\varepsilon_x\,, \qquad (2.7)$$

where subscripts 1 and 2 refer to nucleus 1 and nucleus 2, respectively, in $E_{1,2}$ are excitation energies, $J_{1,2}$ are spins, $\pi_{1,2}$ are parities, $\rho_{1,2}$ are level densities and T_ℓ^x are transmission coefficients (obtained from the optical model using average parameters) for the scattering of particle *x* on nucleus 2. ε_x is the kinetic energy of particle *x*, given by the separation energy as

$$\varepsilon_x = E_1 - E_2\ . \qquad (2.8)$$

2.3.1.2 γ-ray decay

The rate for *E*1, *M*1 or *E*2 transitions is given by

$$R_\gamma d\varepsilon_\gamma = \frac{1}{\hbar}\Gamma_\gamma(\varepsilon_\gamma) = \frac{1}{2\pi\hbar}\frac{\rho_2(E_2,J_2,\pi_2)}{\rho_1(E_1,J_1,\pi_1)}\sum_L \xi_L f_L(\varepsilon_\gamma)d\varepsilon_\gamma\,, \tag{2.9}$$

where L denotes the multipolarity of the γ-ray, ξ_L are constants for transitions between low lying states and f_L are energy dependent strengths [PU77].

2.3.1.3 Fission decay

Fission occurs when a certain critical deformation is reached such that the surface energy is no longer able to overcome the force of electrostatic repulsion. A diagrammatic illustration of the fission decay phenomenon is shown in Fig. 2.2. The total fission width integral over all fragment masses and kinetic energies is obtained from

$$\Gamma_f(E_1,J_1) \sim (2J_1+1)\int_{\varepsilon_f=0}^{E_1-E_{sp}(J_1)} \rho_f(E_1-E_{sp}(J_1)-\varepsilon_f)d\varepsilon_f\,, \tag{2.10}$$

where ρ_f are final level densities to be reached, available at the saddle point, and E_{sp} is the energy of the system at the saddle point. Fission depends on the fission barrier height and the level density at the saddle point [PU77]. We are looking at the energy of the compound nucleus in terms of two distortion parameters, hence the occurrence of a "saddle point".

2.3.2 Resonance reactions

The compound nucleus continuum can be considered as effectively a set of unbound discrete states, unstable against decay, with a spacing between states much smaller than the width of the state, such that

$$\Gamma = \frac{\hbar}{\tau}\,, \tag{2.11}$$

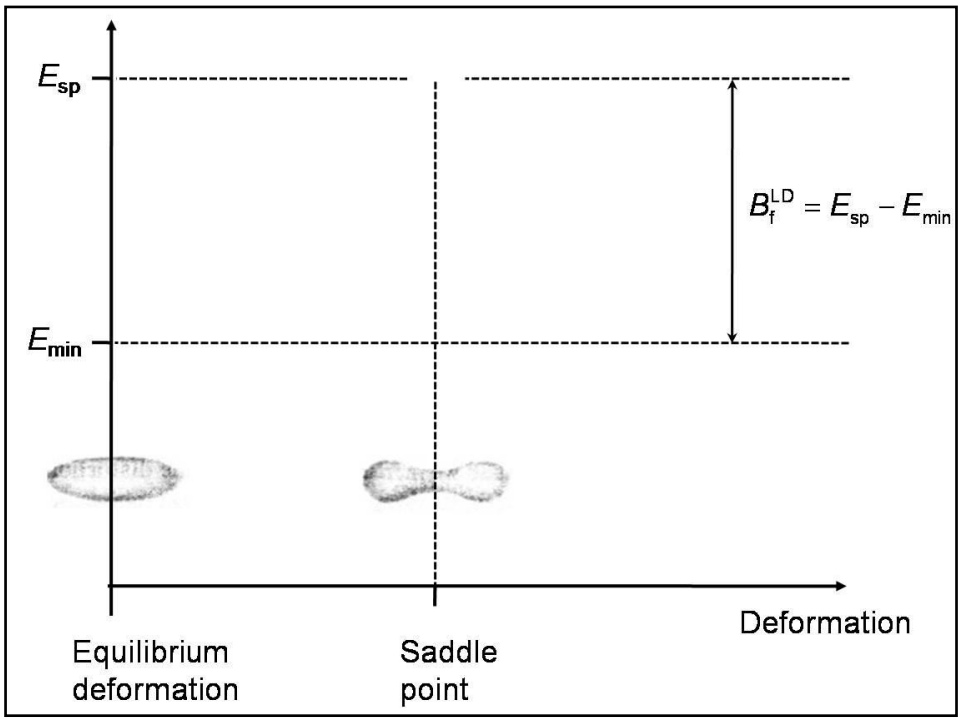


Figure 2.2 An illustration of fission decay of a compound nucleus.

where Γ is the width of state, $\hbar = h/2\pi$ with h being Plank's constant and τ is the decay lifetime.

In contrast, bound states studied in direct reactions are stable against particle decay and have a lifetime of about 1 ps and width of approximately 10^3 eV. In this case, the spacing between states is much larger than the width of the state. Between these two extremes is the resonance region populating discrete levels in the compound nucleus. The resonances occur at low incident energy and have small widths as well as large cross-sections. The resonances are also quasi-bound states decaying to an elastic channel, an inelastic channel or by γ-emission. Resonance occurs at an incident energy where the matching point and amplitude of the exterior wave-functions match well (see Fig. 2.3). Resonance at energy E_R with width Γ occurs when the total cross-section σ_t is a maximum. For a reaction illustrated in Eq. (2.5), the shape of a single isolated resonance may be found from the Breit-Wigner formula [KR88]:

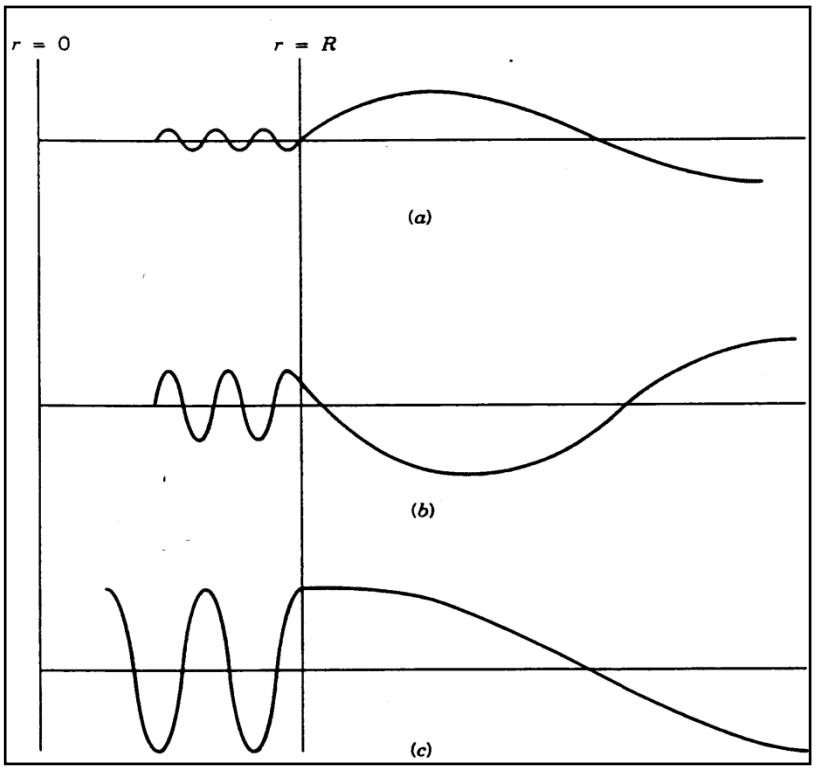


Figure 2.3 (a) Far from resonance, the exterior and interior wave-functions match badly, and little penetration of the nucleus occurs. (b) As the match improves, there is a higher probability to penetrate. (c) At resonance the amplitudes match exactly, the incident particle penetrates easily, and the cross-section rises to a maximum [KR88].

$$\sigma = \frac{\pi}{k^2} g \frac{\Gamma_{aA}\Gamma_{bB}}{(E - E_{\mathrm{R}})^2 + (\Gamma^2/4)} \ , \tag{2.12}$$

$$g = \frac{2I+1}{(2S_a+1)(2S_A+1)} \ , \tag{2.13}$$

$$\vec{I} = \vec{S}_a + \vec{S}_A + \vec{\ell} \ , \tag{2.14}$$

where σ is the resonance cross-section, I is the total angular momentum of the resonance, S_a is the spin of projectile, S_A is the spin of target and ℓ is the orbital angular momentum.

2.4 Optical Model of elastic scattering

By using an interaction potential to describe the nuclear scattering, one can gain a greater insight into the mechanism of elastic scattering (i.e at the level of the averaged potential in the nucleus). The description encompasses partial transparency, surface effects, additional features like spin-orbit coupling and so on. The model makes the assumption that an imaginary part of the potential can account for the presence of reaction channels by absorption of incident flux, and simulates the effect of the non-elastic channels. The model is phenomenological in that the interaction potential is not obtained from fundamental considerations but from a fit to the data or by some other *ad hoc* method.

The two-body interaction potential $U(r)$ represents the many-body interaction between colliding nuclei, where for charged spinless nuclei:

$$U(r) = U_{\mathrm{C}}(r) + U_{\mathrm{N}}(r) \tag{2.15}$$

where $U_{\mathrm{C}}(r)$ is the repulsive Coulomb interaction (long range) and $U_{\mathrm{N}}(r)$ is the attractive nuclear interaction (short range). The scattering potential is complex, with the general form,

$$U_{\mathrm{N}}(r) = V(r) + iW(r), \tag{2.16}$$

where $V(r)$ is the real part, which is responsible for elastic scattering and $iW(r)$ is the imaginary part, which is responsible for absorption of incoming flux into non-elastic-scattering channels.

Generally, a form which is physically plausible and numerically suitable for heavy-ion scattering, referred to as a Woods-Saxon form, is chosen:

$$U_{\mathrm{N}}(r) = -\,Vf_{\mathrm{R}}(r) + iWf_{\mathrm{I}}(r)\ , \tag{2.17}$$

$$f_{\mathrm{R,I}}(r) = \left[1 + \exp\left(\frac{r - R_{\mathrm{R,I}}}{a_{\mathrm{R,I}}}\right)\right]^{-1}, \tag{2.18}$$

where V is the real well depth, $R_{\mathrm{R,I}} = R_{0\mathrm{R,I}}(A_1^{1/3} + A_2^{1/3})$ is the real (imaginary) radius and $a_{\mathrm{R,I}}$ is the real (imaginary) diffuseness.

The imaginary part may be the derivative Woods-Saxon given by

$$W(r) = -W_0 \frac{d}{dr}\left[1 + \exp\left(\frac{r - R_{\mathrm{I}}}{a_{\mathrm{I}}}\right)\right]^{-1} \tag{2.19a}$$

$$= -W_0 4\exp\left(\frac{r - R_{\mathrm{I}}}{a_{\mathrm{I}}}\right)\left[1 + \exp\left(\frac{r - R_{\mathrm{I}}}{a_{\mathrm{I}}}\right)\right]^{-2}, \tag{2.19b}$$

where W_0 is the imaginary well depth, $R_{\mathrm{I}} = R_{0\mathrm{I}}(A_1^{1/3} + A_2^{1/3})$ is the imaginary radius and a_{I} is the imaginary diffuseness. In this case, the imaginary potential is surface peaked since "valence" nucleons at the surface can easily participate in nuclear reactions (Pauli-exclusion principle prevents tightly bound nucleons in the interior from participating) [AU78].

The Coulomb part for charged particle scattering has the form

$$U_{\mathrm{C}}(r) = \frac{z_1 z_2 e^2}{r} \qquad \text{for} \quad r > R_{\mathrm{C}} \tag{2.20a}$$

$$= \frac{z_1 z_2 e^2}{2R_{\mathrm{C}}}\left(3 - \frac{r^2}{R_{\mathrm{C}}^2}\right) \qquad \text{for} \quad r \le R_{\mathrm{C}} \tag{2.20b}$$

$$R_{\mathrm{C}} = \left(\frac{5}{3}\langle r^2 \rangle\right)^{\frac{1}{2}}, \tag{2.21}$$

where z_1 is the projectile (usually taken as point charge) atomic number, z_2 is the target atomic number, R_{C} is the equivalent uniform value which reproduces the observed rms charge radius and $\langle r^2 \rangle$ is the mean-square charge radius (from electron scattering) [WA04].

The Woods-Saxon potential was again used in the present study, so as to have a clear comparison with already existing literature data from [BR61, CA81]. A

projectile of mass a and energy E_{Lab} incident upon a target of mass A obeys the centre-of mass Schrödinger equation

$$-\left(\frac{\hbar^2}{2\mu}\right)\nabla^2\psi = (E-U)\psi\,, \tag{2.22}$$

where μ is the reduced mass, given by

$$\mu = \frac{aA}{a+A} \tag{2.23}$$

and E is the centre-of-mass energy, given by

$$E = E_{\text{c.m.}} = E_{\text{Lab}}\left(\frac{A}{a+A}\right). \tag{2.24}$$

After performing the usual decomposition into partial waves, assuming that the potential U is a function of r alone, the radial wave-equation becomes

$$\left\{\frac{d^2}{dr^2} + k^2\left(1-\frac{U(r)}{E}\right) - \frac{\ell(\ell+1)}{r^2}\right\} f_\ell(kr) = 0\,, \tag{2.25}$$

where k is the wave number, defined as $k = (2\mu E/\hbar^2)^{1/2}$ and $f_\ell(kr)$ is the radial wave function for a particular angular momentum value ℓ of relative orbital motion [AU78]. The third term in Eq. (2.25) is refered to as the centrifugal term pushing the projectile and target away from each other.

Equation (2.25) results from the expansion of wave functions in terms of Legendre polynomials. An explicit form for $U_{\text{C}}(r)$ and $U_{\text{N}}(r)$ is required to solve Eq. (2.25). On solving the radial wave-equation numerically, at large r the nuclear field is negligible and numerical solutions of $f_\ell(kr)$ are matched to known Coulomb wave-functions to determine the nuclear phase shifts δ_ℓ. All the information of the scattering process is contained in δ_ℓ, which is complex since $U(r)$ is complex. The nuclear phase shift, δ_ℓ, is related to the scattering amplitude, $f(\theta)$, as follows:

$$f(\theta) = \frac{1}{2ik}\sum_{\ell=0}^{\infty}(2\ell+1)(S_\ell - 1)\, P_\ell(\cos\theta)\ , \tag{2.26}$$

$$S_\ell = \exp(2i(\sigma_\ell + \delta_\ell))\,, \tag{2.27}$$

where S_ℓ is the elastic scattering S-matrix and σ_ℓ are Coulomb phase shifts which are known analytically. It follows then that

$$e^{2i(\sigma_\ell+\delta_\ell)} - 1 = (e^{2i\sigma_\ell} - 1) + e^{2i\sigma_\ell}(e^{2i\delta_\ell} - 1) \tag{2.28}$$

and hence,

$$f(\theta) = f_{\mathrm{C}}(\theta) + f_{\mathrm{N}}(\theta)\,, \tag{2.29}$$

where $f_{\mathrm{C}}(\theta)$ is the Coulomb scattering amplitude and $f_{\mathrm{N}}(\theta)$ is the nuclear scattering amplitude.

The complex scattering amplitudes $\eta_\ell = e^{2i\delta_\ell}$ are obtained and a six parameter model results. It should be noted that the reflection coefficients are defined as $|\eta_\ell|$ A fit to elastic scattering data is obtained by varying one or more of the six optical model parameters, namely, V_0, $R_{0\mathrm{R}}$, a_{R}, W_0, $R_{0\mathrm{I}}$ and a_{I}, and the elastic scattering cross-section is obtained from

$$\frac{d\sigma}{d\Omega} = \frac{1}{4k^2}\left|\sum_{\ell=0}^{\infty}(2\ell+1)\, i(1-\eta_\ell)P_\ell(\cos\theta)\right|^2 . \tag{2.30}$$

All of the information for elastic scattering resides in η_ℓ [JA70].

2.4.1 Identical particle scattering

For identical particle scattering the entrance channel is symmetric. In describing the symmetry of the wave functions of such systems, some important quantum-mechanical considerations are taken into account. The wave-function has to be symmetric under the interchange of any two bosonic (integer spin) particles and

antisymmetric under the interchange of fermionic (half-integer spin) particles.

The differential scattering cross-section for the elastic scattering of two non-identical particles is given by the following expression

$$\frac{d\sigma}{d\Omega} = |f(\theta)|^2, \tag{2.31}$$

where $f(\theta)$ is the scattering amplitude.

However, in the case of identical particles, the situation shown in Fig. 2.4 arises, where two indistinguishable events are possible. The elastic scattering cross-section is obtained, classically, from

$$\frac{d\sigma}{d\Omega} = \frac{d\sigma(\theta)}{d\Omega} + \frac{d\sigma(\pi-\theta)}{d\Omega} \ . \tag{2.32}$$

Because the corresponding amplitudes are added, a proper quantum-theoretical treatment introduces interference. For bosonic systems, the properly symmetrised elastic scattering cross-section is given by the following expression

$$\frac{d\sigma}{d\Omega} = |f(\theta) + f(\pi-\theta)|^2 \tag{2.33a}$$

$$= \frac{d\sigma(\theta)}{d\Omega} + \frac{d\sigma(\pi-\theta)}{d\Omega} + 2\text{Real}(f(\theta)\, f(\pi-\theta)^*) \ . \tag{2.33b}$$

The observed cross-section has a highly oscillatory structure due to the interference of the two amplitudes, and it is symmetric about $\theta_{\text{c.m.}} = 90°$ [JA70]. At energies well below the Coulomb barrier, only the Coulomb scattering amplitudes are included in the expression for the cross section. In this case, an analytical expression called the Mott scattering formula describes the scattering [MO30].

The Mott scattering formula is analogous to the Rutherford scattering formula for non-identical particle scattering which is given by:

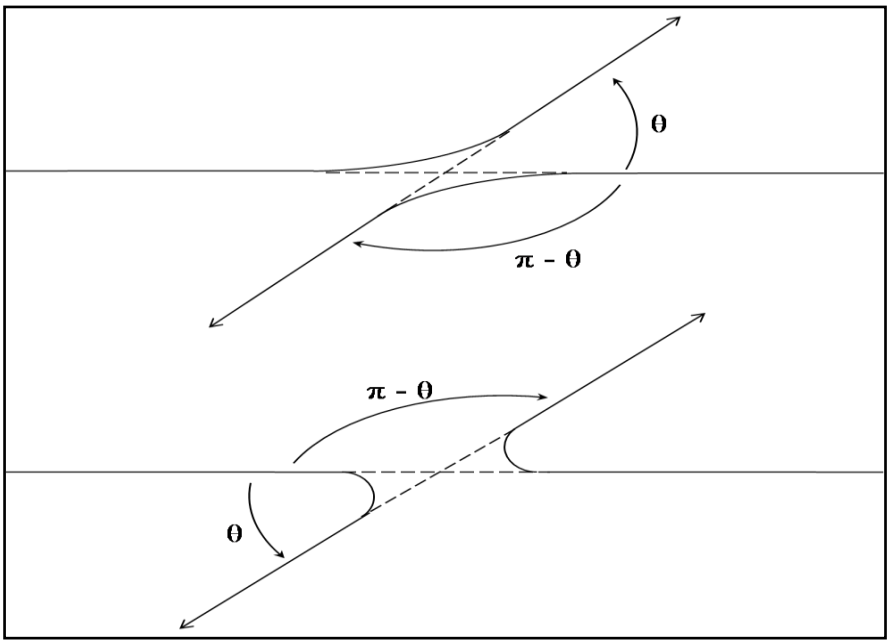


Figure 2.4 Identical particle scattering resulting in two indistinguishable events.

$$\frac{d\sigma}{d\Omega_{\text{c.m.}}} = \frac{z_1 z_2 e^2}{4\pi\varepsilon_0}\left(\frac{1}{4E_{\text{c.m.}}}\right)^2\left(\frac{1}{\sin^4\frac{\theta_{\text{c.m.}}}{2}}\right), \tag{2.34}$$

where $z_1 e$ is the projectile charge, $z_2 e$ is the target charge, $E_{\text{c.m.}}$ is the projectile centre-of-mass energy and $\theta_{\text{c.m.}}$ is the centre-of-mass scattering angle.

The Rutherford scattering formula shows that the Rutherford scattering cross-section is independent of projectile and target spin but depends on scattering angle. For pure Coulomb scattering of point charges (or homogenously charged spheres below the Coulomb barrier), the Rutherford scattering cross-section of Eq. (2.34) becomes the Mott scattering cross-section for identical particle scattering, given by the expression [WA04]:

$$\left.\frac{d\sigma}{d\Omega_{\text{c.m.}}}\right)_I = \frac{\eta^2}{4k^2}\left\{\csc^4\frac{\theta_{\text{c.m.}}}{2} + \sec^4\frac{\theta_{\text{c.m.}}}{2}\right.$$

$$\left. + \frac{(-)^{2I}}{2I+1} 2\cos\left(\eta \ln\tan^2\frac{\theta_{\text{c.m.}}}{2}\right)\csc^2\frac{\theta_{\text{c.m.}}}{2}\sec^2\frac{\theta_{\text{c.m.}}}{2}\right\}, \qquad (2.35)$$

where $\eta = z_1 z_2 e^2 \mu / \hbar^2 k$ is the dimensionless Sommerfeld parameter and k is the wave number. The third term of Eq. (2.35) is the interference term, which depends on the projectile or target spin, *I*.

2.5 Δ*E*-*E* detector

One of the most common techniques for nuclear particle identification is the Δ*E*-*E* method where the specific energy loss (Δ*E*) and the residual energy (*E*) of the particles are measured. The energy loss of charged particles passing through a thin Δ*E* detector can be calculated theoretically by the Bethe-Bloch formula [LE87]:

$$-\frac{dE}{dx} = 2\pi N_{\text{A}} r_{\text{e}}^2 m_{\text{e}} c^2 \rho \frac{Z}{A}\frac{q^2}{\beta^2}\left\{\ln\left(\frac{2m_{\text{e}}\gamma^2 v^2 W_{\max}}{I^2}\right) - 2\beta^2 - \delta - 2\frac{C}{Z}\right\}, \qquad (2.36)$$

where

$2\pi N_A r_e^2 m_e c^2 = 0.1535$ MeVm^{2}kg^{-1} is a constant,

N_{A} is Avogadro's number,

r_{e} is the classical radius of the electron,

m_{e} is the mass of the electron,

c is the speed of light,

ρ is the density of the absorbing material,

Z is the atomic number of the absorbing material,

q is the charge of the incident particle (electron units),

A is the atomic mass of the absorbing material,

β is the ratio of the velocity of incident particle to that of light (v/c),

$\gamma = 1/\sqrt{1-\beta^2}$ is the relativistic factor,

W_{max} is the maximum energy transfer in a single collision,

I is the mean excitation potential,

δ is the density correction and

C is the shell conversion.

For non-relativistic particles, $v^2 = (2E/m)$ with the logarithmic term varying slowly with energy. Neglecting C and δ a simplification of Eq. (2.36) results as

$$\frac{dE}{dx} \propto \frac{mq^2}{E}, \tag{2.37}$$

where m is the mass of the incident particle. As it travels through a gas, a particle loses energy ΔE and its residual energy E is collected by a stop detector as the particle comes to rest. Equation (2.37) is used to identify nuclei through the use of a gas-ionisation detector. A measure of mq^2 can be found from the product $E(dE/dx)$, with the mq^2 being unique for light isotopes up to the α-particle mass.

CHAPTER 3

Experimental Details, Data Analysis and Discussion

In this chapter, descriptions of the experimental details are given for the two analyser magnet calibration methods and the $^{16}O + ^{16}O$ elastic scattering measurements. Descriptions of data analyses as well as discussions are also given. A schematic layout of the Nuclear Physics beam line (C-Line) at iThemba LABS (Gauteng) and associated equipment is shown in Fig. 3.1. Both methods of EN tandem energy calibration used the large 30 inch diameter Ortec scattering chamber and the measurement of $^{16}O + ^{16}O$ elastic scattering angular-distribution took advantage of the high-resolution ΔE-E gas ionisation detector coupled to the small scattering chamber at the end of the beam line.

3.1 Layout of the Nuclear Physics beam line (C-line)

The C-line (see Fig. 3.1) is coupled to the switcher magnet, which directs positive ion beams from the accelerator analysing magnet to the respective beam lines. After switching, the beam is directed through Faraday cup 1, which allows for the accurate monitoring of ion beam current. The quadrupole magnet focuses the beam down the C-line. The function of the liquid nitrogen cryo-trap is to inhibit build-up of surface layers of carbon or silicon on the target; originating from the diffusion pumps upstream. The line slits are adjusted manually and together with the entrance collimators of the large or small scattering chambers, determine the beam angular divergence at the corresponding target.

From the beam optics geometry, the focusing through line slits and collimators results in a beam angular divergence of 0.2°. The large scattering chamber is 30 inches in diameter, and can accommodate up to 5 surface barrier detector

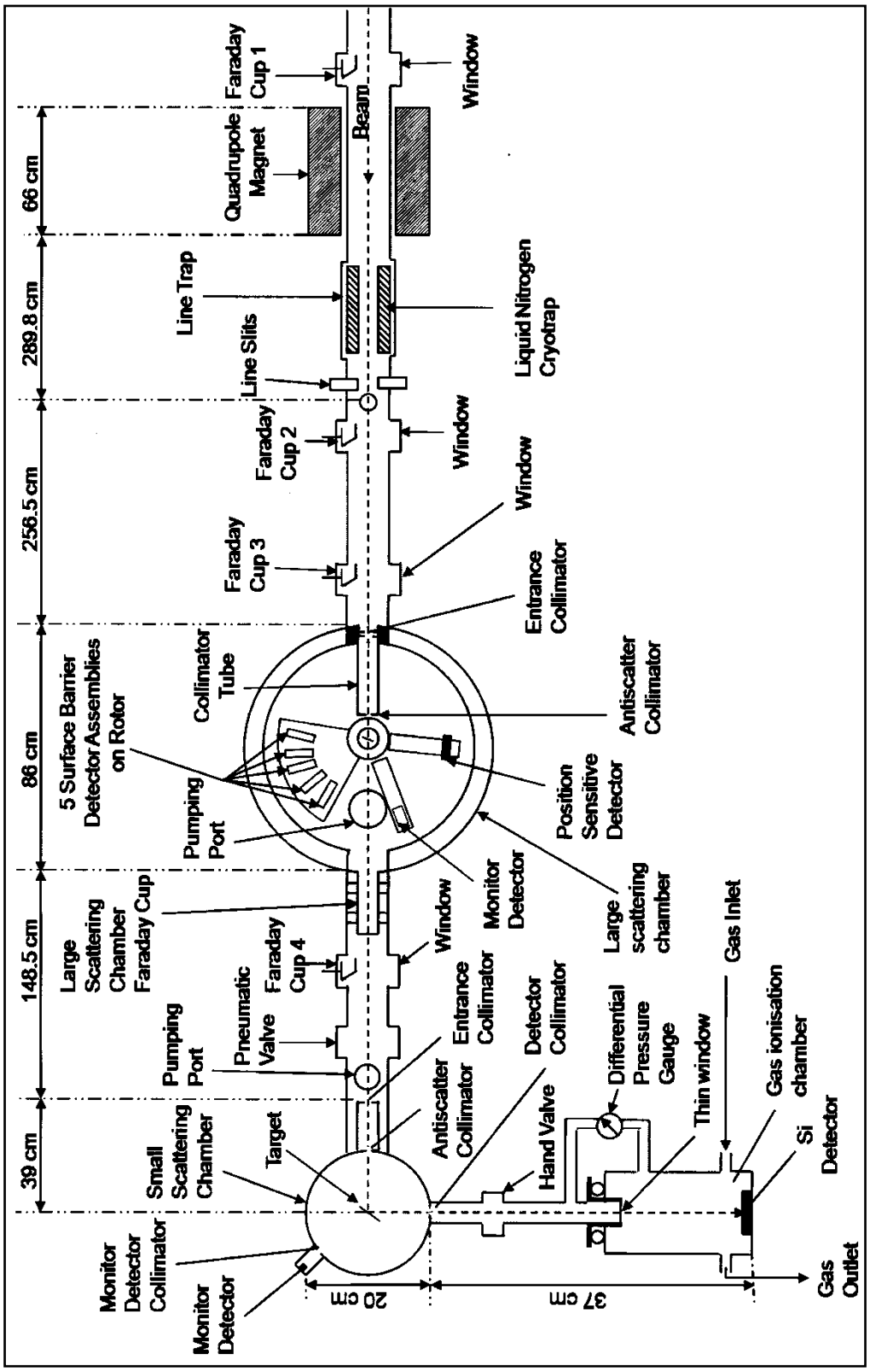


Figure 3.1 Plan view of the C-Line at the 6 MV EN tandem accelerator laboratory of iThemba LABS (Gauteng).

assemblies on a rotor with 5 slots 10° apart. In addition, a single slot independent rotor can be used for coincidence measurements. The small scattering chamber has a diameter of 20 cm and its top part can be rotated around the target holder. This movable top part of the small scattering chamber is connected to the gas-ionisation detector via a port carrying the detector collimator. The top part of the chamber tilts out of the horizontal plane on its base, allowing measurements to be made on either side of the 0° scattering angle from -20° to +135°. The scattered products detection angle has an error of ±0.5° due to the Δ*E*-*E* detector collimator.

Apart from monitoring beam currents, Faraday cups can be closed remotely from the control room, thus blocking the beam from passing through a certain part of the C-Line, allowing for troubleshooting in the part without beam to take place. The beam blocking also allows for changing of pre-loaded targets on the target ladder, which is done manually.

3.2 Refurbished accelerator inflection magnet scan

Refurbishment of the 6 MV EN tandem accelerator of iThemba LABS (Gauteng) has been completed and some of the major changes made are as follows: the belt charging system was replaced with a pelletron charging system, new axial electric and spiralled magnetic field tubes were installed, the gas stripper was converted to a recirculating one with High Voltage (HV) terminal pumping, new high-voltage grading resistors and resistor mounts were installed, new centralised computer control systems and customised software were also developed and put into operation. The injection negative ion system was also redesigned and the ion source was upgraded from an 860A to 860C sputter ion-source which gives a more focused beam.

The newly upgraded 860C sputter ion source with a graphite target was used to carry out an inflection magnet scan. More details on ion source target preparation can be obtained from [MI89]. The inflection magnet bends the negative ion beam

from the ion source through 30° before injection into the accelerator. Using a source extraction voltage (V_{ext}) of 23.5 kV which essentially determines the energy of the negative ion beam emitted by the sputter ion source, the negative-ion beam current at the low-energy Faraday cup was measured, noting corresponding current flowing through the inflection magnet after every variation.

Using the relationship

$$F_{em} = q\vec{v} \times \vec{B}_{in} \ , \tag{3.1}$$

where F_{em} is the electromagnetic force experienced by a charged ion passing through the inflection magnet, q is the ion charge, v is the ion velocity and B_{in} is the magnetic field of the inflection magnet.

$$B_{in} \propto I_{in} \ , \tag{3.2}$$

where I_{in} is the current through the inflection magnet, which can therefore be interchanged with B_{in} in Eq. (3.1). Noting that

$$E = qV = \frac{1}{2}mv^2 \tag{3.3}$$

this leads to

$$v = \sqrt{\frac{2qV}{m}} \ , \tag{3.4}$$

where E is the ion kinetic energy, V is the accelerating voltage and m is the ion mass. Substituting Eqs. (3.2) and (3.4) into Eq. (3.1) yields

$$F_{em} \propto q\sqrt{\frac{2qV}{m}} I_{in} \ , \tag{3.5}$$

which can be rearranged to give

$$F_{em} \propto q\sqrt{2qV}\,\frac{I_{in}}{\sqrt{m}} \ , \tag{3.6}$$

Therefore, a final expression can be written relating the inflection magnet current to the square root of the mass at constant charge and accelerating voltage:

$$I_{\text{in}} = k\sqrt{m} \propto \sqrt{m} \ , \tag{3.7}$$

where *k* is a constant, which was determined experimentally to have a value of 3.95. Equation (3.7) was used to do the conversion of inflection magnet current to ion masses. Since the ions produced by the sputter ion source all carry a single negative charge, this fact can be used to differentiate between the various species produced, as shown in Fig. 3.2.

This exercise gave an indication of where to set the inflection magnet current in order to obtain most of the required light heavy-ion beams up to about mass number 19, which are the most commonly used ion beams in nuclear structure studies at the 6 MV EN tandem accelerator of iThemba LABS (Gauteng).

The author and co-worker presented this work in a poster at the 53rd Annual Conference of the South African Institute of Physics, in the Nuclear, Particle and Radiation Physics specialist group, held in July 2008 at the University of Limpopo [JI08].

3.3 EN tandem accelerator analyser magnet calibration

In this section, descriptions are given of the procedures followed in the two calibration methods. The data collection and analysis techniques used in the tandem analyser calibration are described, including the error analyses. A desription is given of how the two calibration methods were combined to arrive at the final analyser magnet constant. A discussion concerning the calibration methods is also included here.

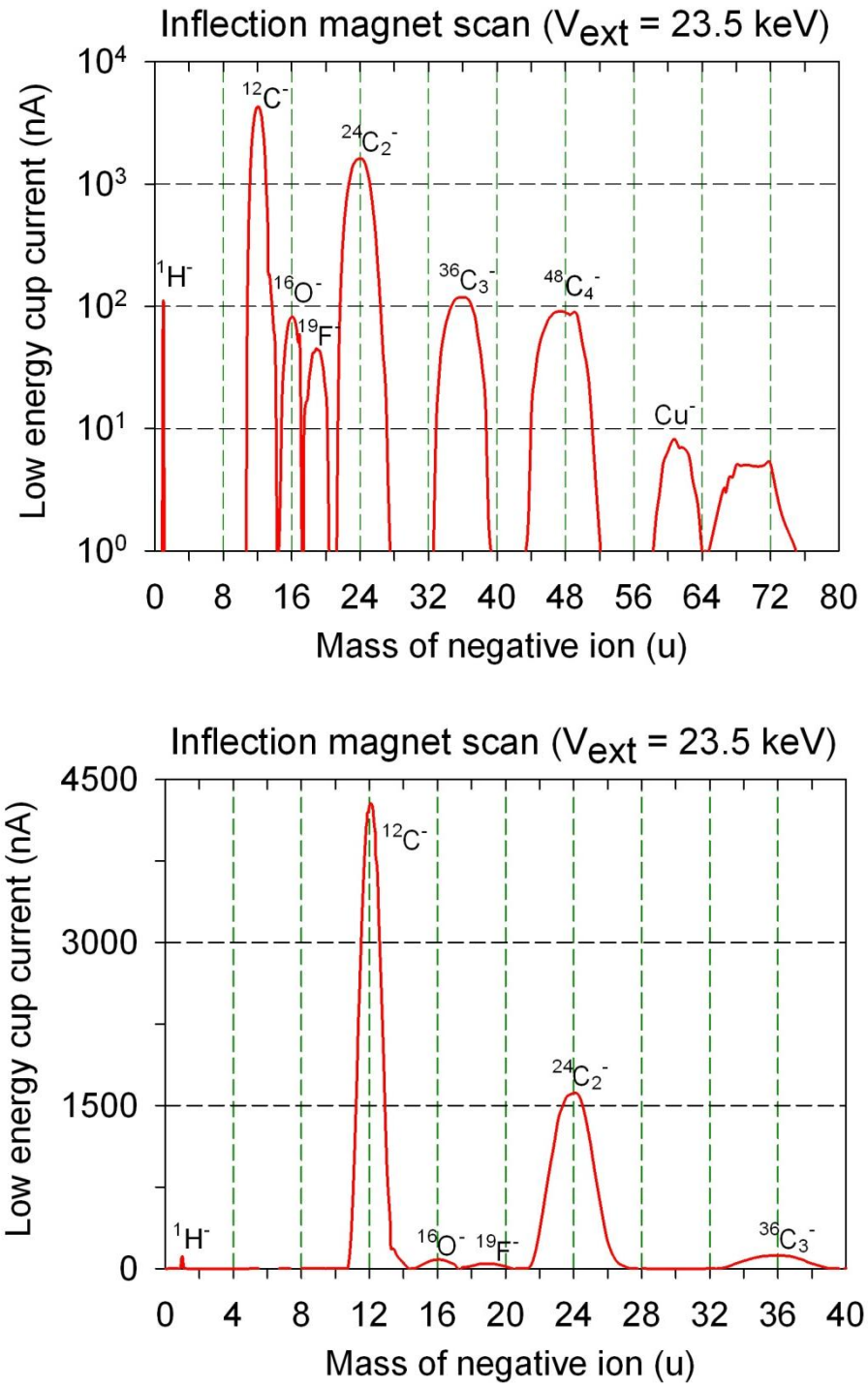


Figure 3.2 *Upper:* Log plot of ion source species identified, using a graphite target in an 860C negative sputter ion-source with source extraction voltage (V_{ext} = 23.5 keV). *Lower*: Linear plot of ion source species identified, using a graphite target in an 860C negative sputter ion-source with source extraction voltage (V_{ext} = 23.5 keV).

3.3.1 Method 1: ^{27}Al(p,n)^{27}Si reaction

The first method of analyser magnet calibration involved the use of the ^{27}Al(p,n)^{27}Si resonance reaction to determine the proton beam energy from the known sharp neutron-emission threshold of E_p = 5.802 ± 0.001 MeV [MA66, RI66, OV69, NA77]. Figure 3.3 shows part of the experimental set-up for this calibration method. In this case, a model 860A negative sputter ion source was used to produce the H^- ion beam from pure powdered titanium hydride. Full details on beam preparation can be obtained from [MI89]. The H^- ion beam was accelerated by the 6 MV EN tandem accelerator of iThemba LABS (Gauteng). A target of ^{27}Al, mounted at the end of the large scattering chamber Faraday cup (Fig. 3.3) was bombarded by the proton beam.

The neutrons were detected with a standard BF_3 detector, whose operation is discussed in Sections 3.3.1.1 and 3.3.1.2. The neutron count readings were observed from a camera (see Fig 3.3), which was connected to a computer screen in the Control Room, since precautions had to be taken not to enter the Target Room while beam was on target. This was done to avoid neutron irradiation of the experimentalists. The ^{27}Al target was thick enough (0.27 mm) to stop the proton beam and was connected to a current integrator circuit. The magnetic field within the analyser magnet was measured with a proton Nuclear-Magnetic-Resonance (NMR) probe placed near the midpoint of the beam trajectory within the analyser magnet.

The proton beam energy was set below the threshold energy, by approximately 150 keV. After achieving beam-on-target, the neutron yield produced by this energy was obtained. Proton beam energy was varied in steps of about 25 keV over the threshold, obtaining a measurement of the neutron yield from below to well above the threshold. The beam current was kept at about 30 nA throughout the experiment. A 4-minute neutron background count was obtained prior to putting beam-on-target, each time the beam energy was varied. The reaction product neutron counting period was 10 minutes for every set proton beam energy. Values for these measurements are shown in Table A1 in the Appendix.

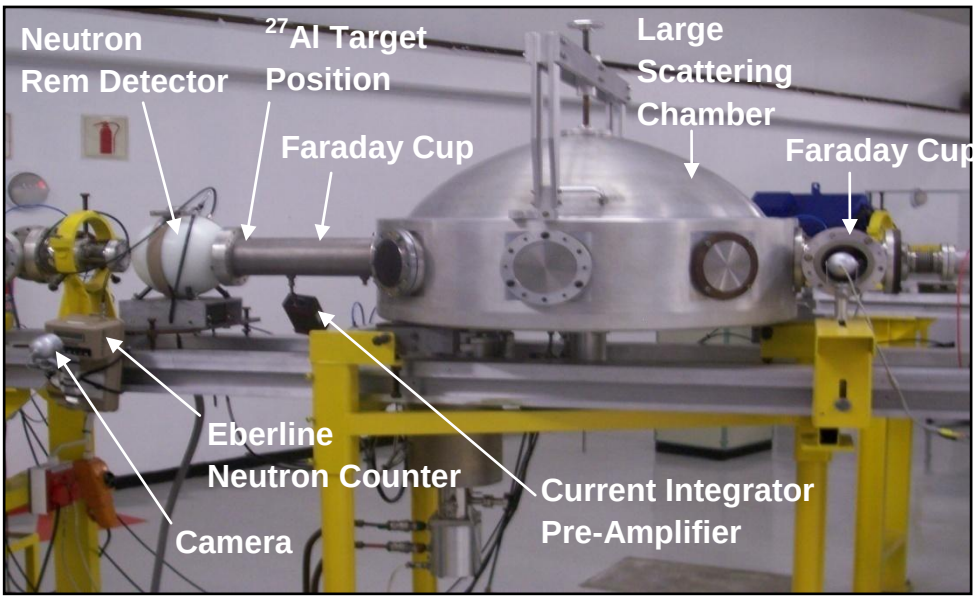


Figure 3.3 Part of the C-line experimental set-up to measure neutron yield from the $^{27}Al(p,n)^{27}Si$ reaction.

3.3.1.1 Eberline BF_3 Neutron Rem Detector

The Model NRD neutron rem detector (see Fig. 3.4) is a nine-inch diameter, cadmium-loaded polyethylene sphere with a BF_3 tube in the centre. The detector has an energy response which closely follows the theoretical dose from neutrons over the energy range from 0.025 eV (thermal) to about 10 MeV. The BF_3 tube allows excellent gamma rejection of up to 500 R/h dependent on high voltage setting. The counting instrument must supply high voltage adjustable from approximately 1500 V to 2500 V. A single coaxial cable, which may be any length up to a maximum of 100 feet, depending on the counting instrument's input sensitivity, connects the detector to the electronics. However, it should be kept as short as practical for maximum noise rejection. The plateau region is approximately 200 V with a slope of about 5% per 100 V. The detector mass is about 6.3 kg [TH91]. The operating voltage was set at 1680 V as determined by the manufacturer. The neutron rem detector is designed to operate in conjunction with a microcomputer-based portable radiation survey instrument, the Eberline Smart Portable (Model ESP-1), whose operation is described in Section 3.3.1.2.

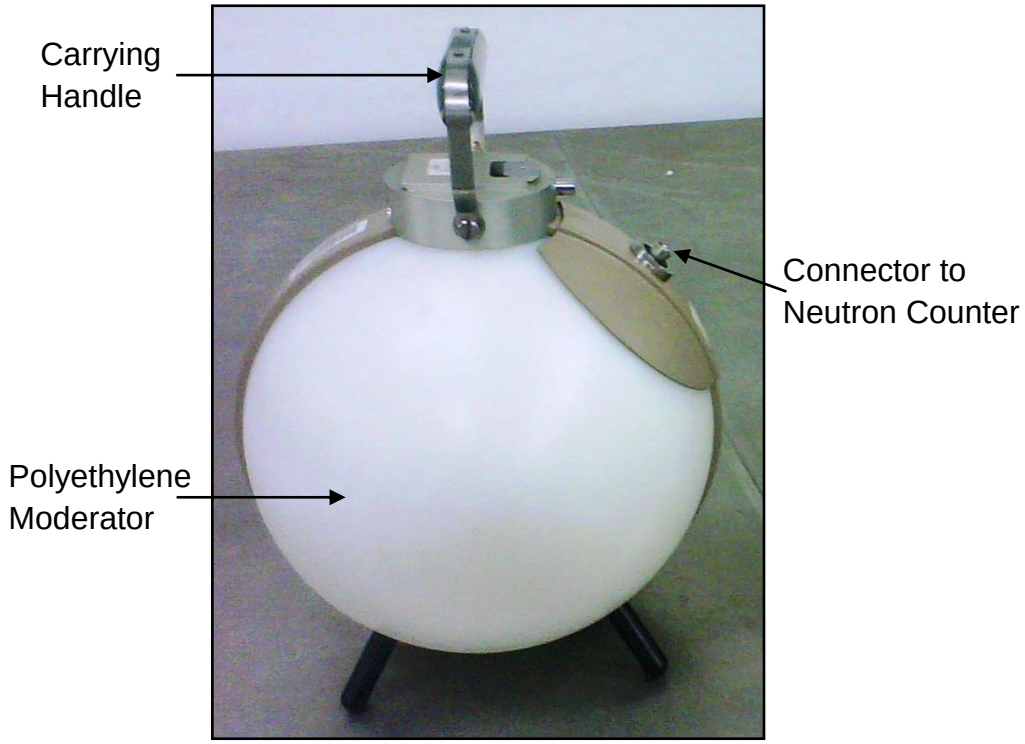


Figure 3.4 Photograph of the Eberline Neutron Rem Detector which was used to detect neutrons in the $^{27}Al(p,n)^{27}Si$ reaction.

3.3.1.2 Eberline Model ESP-1 Neutron Counter

The Eberline Model ESP-1 (see Fig. 3.5) is a microcomputer-based portable radiation survey instrument designed to operate with most Eberline radiation detectors. The ESP-1 can display the data from these detectors in radiation units as selected and calibrated by the user. The instrument's most important function is the delivery of accurate information to the operator efficiently and rapidly. The detector connected to the ESP-1 is selected to optimize its output for the radiation of interest and provides the pulse signal to the electronics for counting, where the pulse rate from the detector is proportional to the radiation-field intensity at the detector. The high voltage supply provides the bias voltage to the detector as required for proper operation. The linear, fixed-gain, multi-stage design amplifier amplifies the signal from the probe to a usable level at the amplifier output. The discriminator provides a signal on its output only if the signal from the amplifier

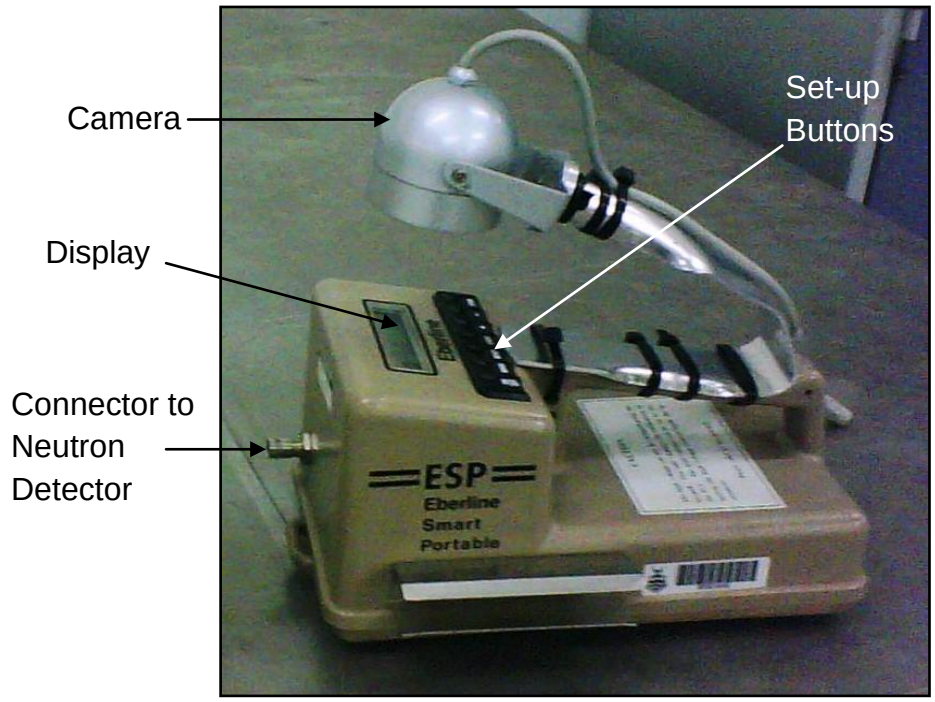


Figure 3.5 Photograph of the Eberline Smart Portable (ESP1) neutron counter which was used in the $^{27}Al(p,n)^{27}Si$ reaction.

exceeds its adjustable threshold and this, in turn, provides a means for counting only the radiation signals and to reject any noise and/or unwanted signals. The microcomputer is an eight-bit device programmed to function as the interface between the ESP-1 operator and the information provided by the radiation detector (probe). Its programme logic and speed of execution allow the ESP-1 to be extremely versatile by applying mathematical functions and logic to its input signals and displaying the results to the operator in an understandable format (technical details supplied by the manufacturer, see Ref. [EB92]).

3.3.1.3 Data analysis

Standard beam current integration techniques were used to normalise between runs as the incident proton beam energy was increased (see Section 3.3.1). Figure 3.6 shows a plot of the normalised neutron yield as a function of NMR frequency. The main error in these measurements was due to the neutron counting statistics.

The net neutron yield was obtained by subtracting a linearly varying background, determined from the yields below threshold. The constant background, together with the upper and lower limits, are indicated in Fig. 3.6.

The net neutron yield raised to the 2/3-power was plotted as a function of NMR frequency as shown in Fig. 3.7. The procedure for determining the neutron threshold energy is dictated by the fact that the yield of s-wave neutrons, i.e, neutrons with zero angular momentum from a thick target, varies as the 3/2-power of the neutron energy, i.e., approximately as $(\Delta E)^{3/2}$, where ΔE is the difference between the bombarding energy and the threshold energy [BE76, MA66].

To obtain the proton NMR frequency corresponding to the neutron emission threshold, a linear extrapolation of the net neutron yield raised to the 2/3-power *versus* NMR frequency plot was used in [OV69, NA77]. Although the 2/3-power linear extrapolation is strictly valid only for $l = 0$ neutron emission where the neutron yield is governed solely by phase space factors, the frequency at zero intercept can be determined without ambiguity if the yield above threshold empirically obeys the 2/3-power law. This is all that is required for calibration purposes. However, a linear fit at the threshold underestimates the threshold NMR frequency, as explained in [BE76] and also indicated in Fig. 3.7. According to the same reference, a fit through the points gives a more accurate value of threshold frequency. In the present study, it was only necessary to use a third order polynomial to obtain a best fit through the data points, as shown in Fig. 3.7.

The $^{27}Al(p,n)^{27}Si$ NMR threshold frequency error bar shown in Fig. 3.7 was obtained by varying the amount of background subtraction, within acceptable upper and lower limits and refitting the corresponding results with new polynomials, resulting in different threshold frequencies depending on the amount of background subtraction. Although the background variation was the same on either side of the threshold frequency, the error bar is asymmetric. Having obtained the threshold frequency f as 22.33965 ± 0.03802 MHz, from the

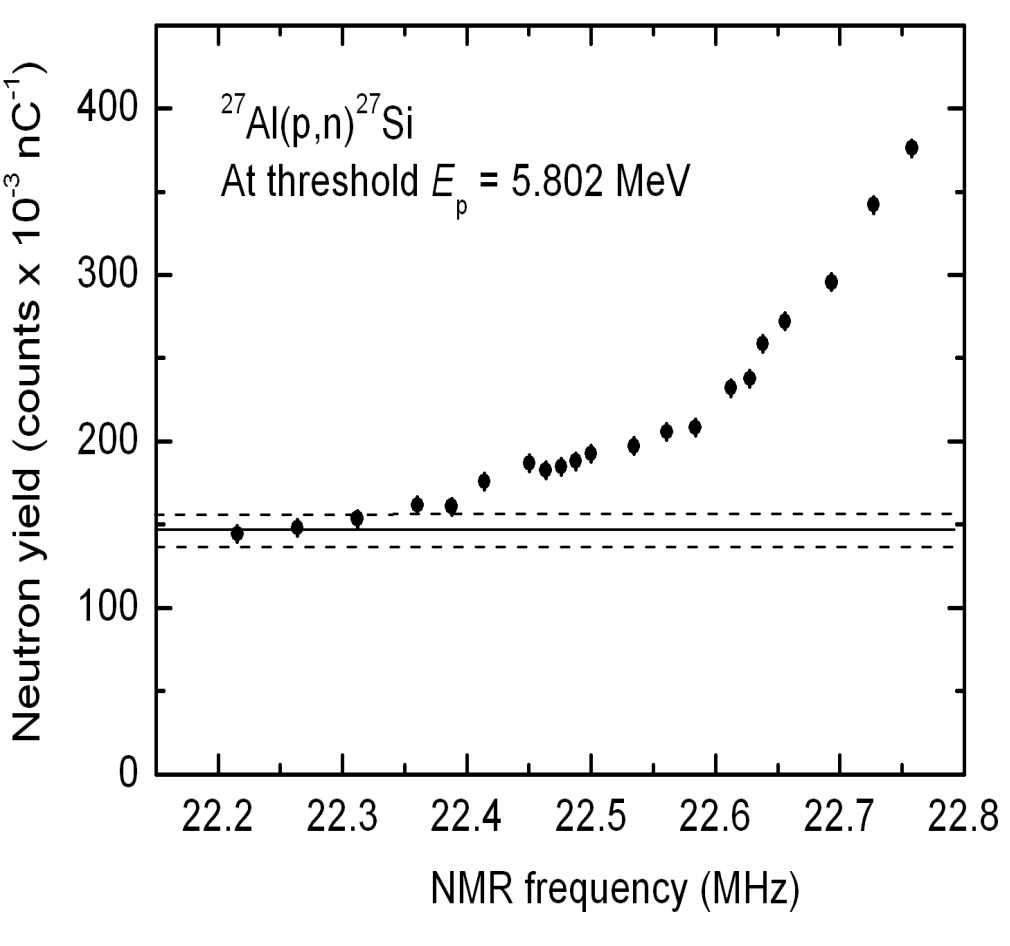


Figure 3.6 Normalised neutron yield for the ^{27}Al(p,n)^{27}Si reaction, plotted as a function of NMR frequency. The constant background is shown by the solid line with the upper and lower limits indicated by the dashed lines.

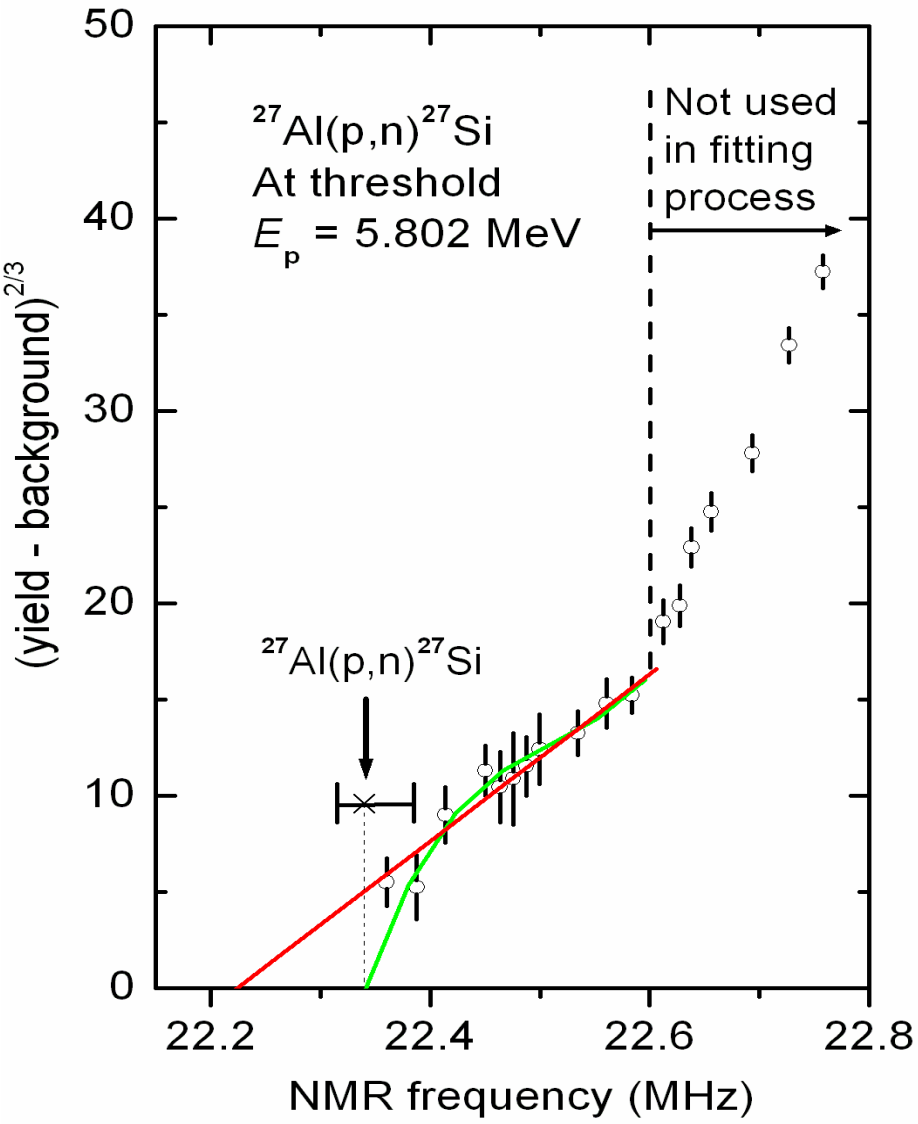


Figure 3.7 Threshold curve for the ^{27}Al(p,n)^{27}Si reaction, showing $(Y\text{-}B)^{2/3}$, where Y is the neutron yield and B is the mean background, plotted as a function of NMR frequency. The error bar on the ^{27}Al(p,n)^{27}Si measurement is determined by the upper and lower limits of background subtraction (see Fig. 3.6).

third order polynomial fit, Eq. (2.3) was used to calculate a value for the analyser magnet constant, K_1 (the subscript 1 refers to calibration method 1). Proton mass (1.007276 u) was used for M, the threshold energy value E (5802 ± 1 keV) was taken from [OV69]. Proton charge value Q was 1e. The value used for c^2 was 931502 keV/u. The analyser magnet constant, K_1 was found to be 11.7467 ± 0.0399 keV.u/MHz^2.

3.3.2 Method 2: $^{12}C(^{16}O,\alpha)^{24}Mg^*$ reaction

After acceleration, the beam was focused into the large scattering chamber, along the C-line (see Fig. 3.1), where it was scattered by a thin self-supporting carbon foil target of areal density approximately 50 µg/cm^2. Figure 3.8 shows energy levels of ^{24}Mg, with low-lying levels being populated in the $^{12}C(^{16}O,\alpha)^{24}Mg^*$ reaction. A silicon surface-barrier detector was used to detect the reaction products, thus obtaining a measured (see Fig. 3.9) alpha-particle energy spectrum from the $^{12}C(^{16}O,\alpha)^{24}Mg^*$ reaction at a laboratory angle as far back as possible (θ_{Lab} = 170° ± 2°). Down stream from the target was a movable thin ^{241}Am α-source which was used to energy calibrate the detector, after obtaining a high energy-resolution spectrum. This spectrum is shown in the upper part of Fig. 3.10. The lower part of Fig. 3.10 shows an enlarged view of the alpha group for the $^{24}Mg^*$ level at 1.369 MeV of excitation bracketed by the main peaks from an ^{241}Am α-source [OL87].

3.3.2.1 Data analysis

Nuclear masses, Q-values, excitation energies and calibration energies were taken from [WA75, LE78]. The energy difference E_{diff} between the known (see Fig. 3.10) energies (E_2 and E_1) of the two main α-peaks was calculated from

$$E_{diff} = E_2 - E_1 \qquad (3.8)$$

Therefore,

E_{diff} = (5486 – 5443) keV = 43 keV.

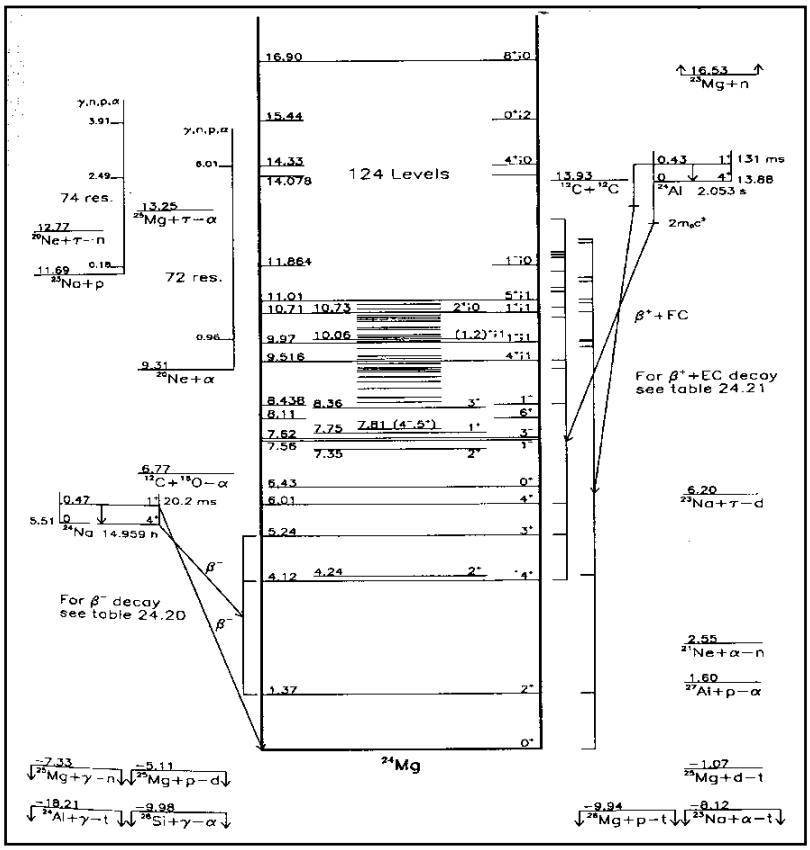


Figure 3.8 Energy levels of ^{24}Mg [EN90].

By performing a Gaussian curve fitting process, the centroids (channel numbers, Ch_1 and Ch_2) of the two main α-peaks were noted. The number of channels between the two main α-peaks Ch_{diff} was obtained from

$$Ch_{\text{diff}} = Ch_2 - Ch_1 \tag{3.9}$$

From Eq. (3.9) we have Ch_{diff} = (1709.705 – 1696.300) Ch = 13.405 Channels. The energy calibration E_{Cal} was hence calculated to be 3.208 keVCh^{-1} through dividing Eq. (3.8) by Eq. (3.9). The position of the bracketed alpha group $Ch_{\text{B}\alpha}$ for the ^{24}Mg* level at 1.369 MeV of excitation was found to be at 1708.40 channels from the centroid of the peak, after a Gaussian curve fitting procedure. The energy of the bracketed α-peak $E_{\text{B}\alpha}$ was obtained from:

$$E_{\text{B}\alpha} = E_{\text{Cal}} * Ch_{\text{B}\alpha}\,. \tag{3.10}$$

On substituting the corresponding numerical values into Eq. (3.10), $E_{\text{B}\alpha}$ was

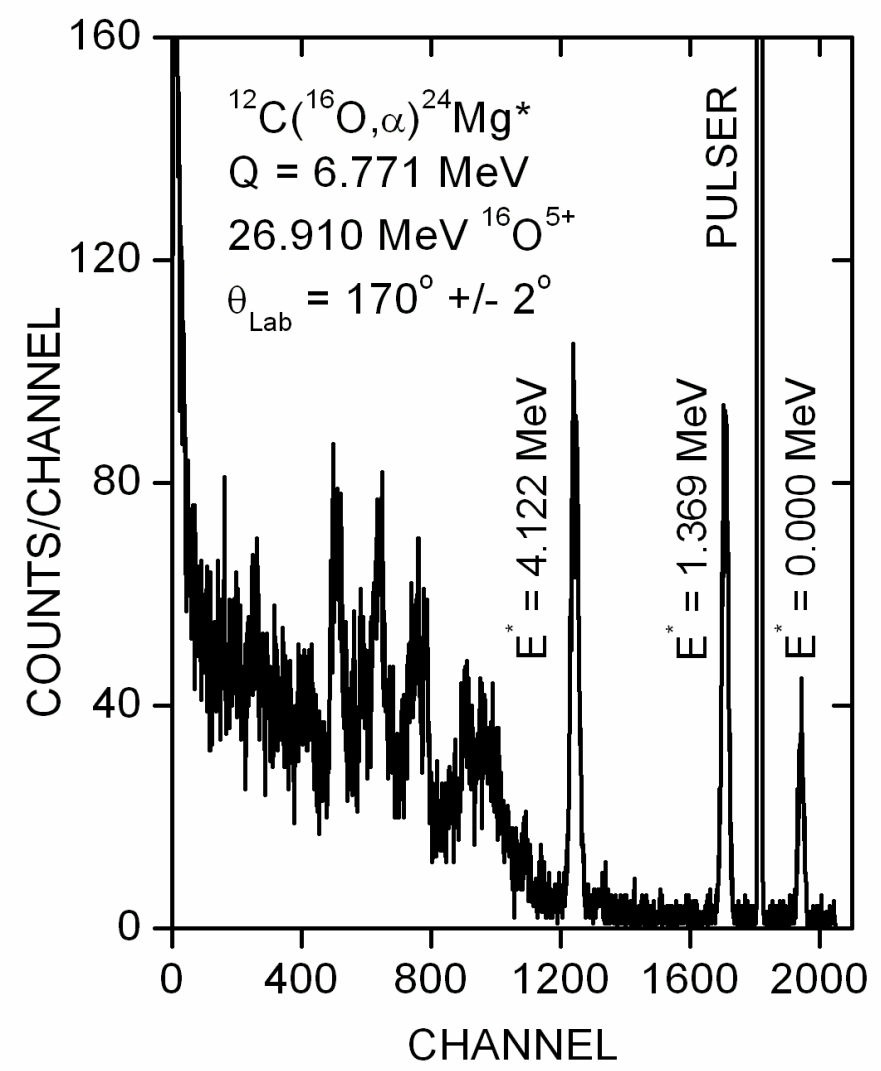


Figure 3.9 Measured energy spectrum from the $^{12}C(^{16}O,\alpha)^{24}Mg^*$ reaction.

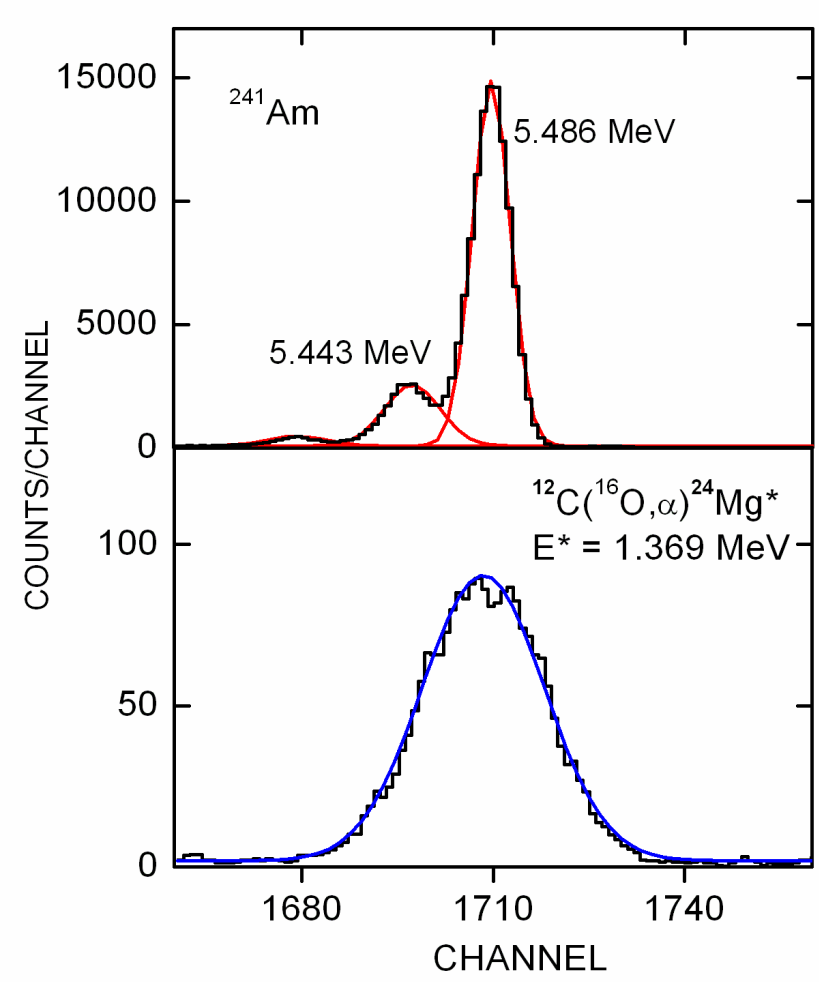


Figure 3.10 *Upper*: Main peaks from an ^{241}Am α-source.
Lower: Enlarged view of the alpha group for the ^{24}Mg* level at 1.369 MeV of excitation. Gaussian curve fittings are shown around each peak.

obtained to be 5.480 MeV. The $^{16}O^{5+}$ beam suffered an average energy loss of about 170 keV in the 50 μg/cm^2 ^{12}C target while the reaction product α-particles lost about 15 keV on average in the target, as calculated from an energy loss computer programme. Using a kinematics computer programme working backwards, with the energy loss in target corrections, showed that the incident $^{16}O^{5+}$ beam energy that led to the 5.480 MeV bracketed α-peak was $E_{Lab}(^{16}O^{5+})$ = 27.206 ± 0.266 MeV.

The error in this beam energy comes mainly from the error in the backward scattering angle which was estimated to be accurate to ± 2°. The energy of the incident beam was then used in conjunction with the frequency reading of the NMR fluxmeter, which was 38.53235 ± 0.01524 MHz, to calculate the analyser magnet constant, K_2 (here, the subscript 2 refers to calibration method 2), using Eq. (2.3). Mass of $^{16}O^{5+}$ was found by subtracting the mass of 5 electrons from the atomic mass of ^{16}O. Thus, the value 15.992172 u was used. The ionic charge Q was 5e. The value used for c^2 was 931502 keV/u. Here, K_2 was found to be 11.7321 ± 0.1146 keV.u/MHz^2.

3.3.3 Combination of the two calibration methods

The final value of analyser magnet constant K was obtained by finding the weighted average of the two constants (K_1 and K_2) from the two calibration methods, based on the assumption that both were a measure of the same analyser magnet constant. Equations 3.11a and 3.11b [BA67] were used to calculate the weighted average K of the analyser magnet constant:

$$K = \frac{1}{(\Delta K_1)^{-2} + (\Delta K_2)^{-2}} \left(\frac{K_1}{(\Delta K_1)^2} + \frac{K_2}{(\Delta K_2)^2} \right), \tag{3.11a}$$

$$\Delta K = \sqrt{\frac{(\Delta K_1)^2 (\Delta K_2)^2}{(\Delta K_1)^2 + (\Delta K_2)^2}}, \tag{3.11b}$$

where ΔK_1, ΔK_2 and ΔK are the errors on analyser magnet constants in Method 1,

Table 3.1 Analyser magnet calibration constant measurements.

Reaction	**Magnet Constant (keV.u/MHz^2)**	**Error (keV.u/MHz^2)**
^{27}Al(p,n)^{27}Si	K_1 = 11.7467	ΔK_1 = ± 0.0399
^{12}C(^{16}O,α)^{24}Mg*	K_2 = 11.7321	ΔK_2 = ± 0.1146
Weighted Average	***K* = 11.7451**	**Δ*K* = ± 0.0377**

Method 2 and weighted average, respectively. Table 3.1 shows a summary of the final results, with their associated errors.

The final value of *K* was incorporated into a Nuclear Magnetic Resonance (NMR) computer programme, which calculates and displays the NMR frequency for a given ion beam. The following parameters are input into the programme: ion beam mass, ionic charge state and beam energy. This programme can be used on a day to day basis to calculate the NMR frequency setting for the NMR fluxmeter, which is connected to the analyser magnet of the accelerator. For example, the NMR frequency setting for the $^{16}O^{5+}$ beam at 30 MeV, used in the elastic scattering study (see Section 3.4) was obtained this way.

The calibration work was presented at the 54th annual conference of the South African Institute of Physics, held in July 2009 at the University of KwaZulu-Natal [KU09], where the author was awarded a prize for the best MSc poster presentation in the Nuclear, Particle and Radiation Physics specialist group.

3.4 Measurement of $^{16}O(^{16}O,^{16}O)^{16}O$ identical particle scattering and check against previous results

Most information about nuclei and nuclear forces is obtained by the relatively indirect and crude means of a scattering experiment: basically, bouncing a particle off a nucleus and seeing what comes out. The scattering experiment is the basic tool which aids our understanding of the nucleus in its ground and excited states and allows us to study unusual nuclei (far from the valley of stability) or in particular excited states.

In this particular experiment, the 30 MeV $^{16}O^{5+}$ beam was provided by the 6 MV EN tandem accelerator of iThemba LABS (Gauteng). A model 860A negative sputter ion source was used to produce the $^{16}O^{-}$ beam. A sputter cathode was prepared by compressing a mixture of powdered alumina (Al_2O_3) and powdered copper in the percentage ratio of about 40:60, respectively. The copper was used to provide conductivity [MI89]. A self-supporting SiO_2 target of approximately 50 μgcm^{-2} areal density, mounted in the small scattering chamber (see Fig. 3.1) was used. An overview of the data measured is shown in Table 3.2. The energy-loss and residual-energy signals were collected and analysed with the use of the CAMAC data acquisition system and an on-line computer.

Table 3.2 Overview of the data measured in $^{16}O(^{16}O,^{16}O)^{16}O$ reaction.

E_{Lab} (MeV)	$E_{c.m.}$ (MeV)	Projectile and Target	Detected Nucleus	θ_{Lab} (deg.)	$\theta_{c.m.}$ (deg.)
30	15	$^{16}O + SiO_2$	^{16}O	15.5 – 45.5	31.0 – 91.0

3.4.1 Use of the Δ*E*-*E* gas-ionisation detector

Figure 3.11 shows a schematic diagram of the Δ*E*-*E* gas-ionisation detector used

to identify the scattered reaction products and determine kinetic energies. The scattered ion beam entered the iso-butane gas filled chamber through a thin (2 μm) mylar window. The ions, having lost some energy (ΔE) to the gas because of ionisation of gas molecules, were finally stopped by a solid-state silicon surface-barrier detector at the end of the chamber, where the residual energy (E_{Stop}) was deposited and measured.

Although somewhat more complicated to handle, gas-ionisation detectors avoid several shortcomings of solid state ΔE detectors: the main advantage of using a ΔE-E gas-ionisation detector for particle identification is that data for all channels, i.e elastic and reaction, may be collected simultanously; by adjusting the gas pressure, the thickness of the ΔE detector can be varied according to the requirements of a given particular experiment. Independent of the thickness, the homogeneity of a ΔE detector can be made better than 1% for entrance windows of several cm^2, which is still not achieved by very thin solid-state detectors; ionisation chambers are not subject to radiation damage.

The optimum operating conditions which were set up for use of the ΔE-E gas-ionisation detector were determined separately [JI09]. These were arrived at by performing an experiment to determine the operating plateau region of the detector using iso-butane gas. The values for V_{C}, V_{G}, V_{A}, V_{EStop} and V_{EMonitor} being the bias voltages on cathode, Frisch grid, anode, stop detector and monitor detector, repectively, are given in Table 3.3.

Table 3.3 Optimum operating conditions for the ΔE-E gas-ionisation detector.

Isobutane Pressure (kPa)	V_{C} (V)	V_{G} (V)	V_{A} (V)	V_{EStop} (V)	V_{EMonitor} (V)
1	-30	30	230	75	150

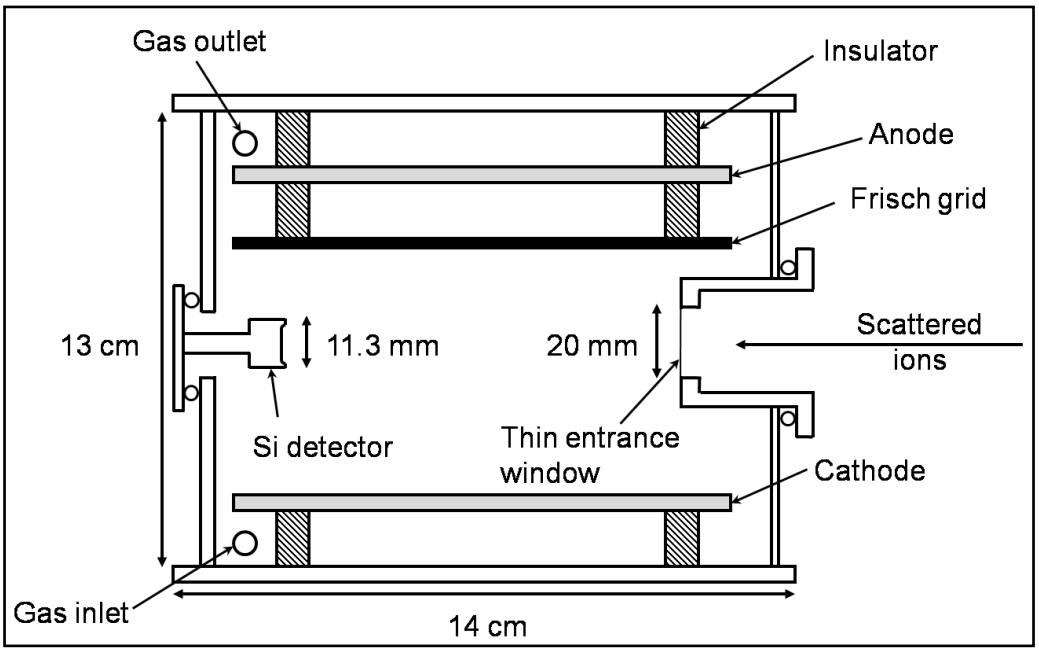


Figure 3.11 Schematic diagram of the Δ*E*-*E* gas-ionisation detector.

3.4.2 Description of electronics set-up

An electronics block diagram showing the arrangement of the components used in this experiment is shown in Fig. 3.12. The preamplifiers of the monitor and *E*-detectors each had conversion gains of 20 mV/MeV and that of the Δ*E*-detector had a conversion gain of 45 mV/MeV. The function of the preamplifiers was to amplify weak signals induced at the detectors, before transmission over a coaxial cable approximately 40 m long from the Target Room to the Data Room. After amplification by spectroscopy amplifiers, the unipolar outputs were fed into Analogue-to-Digital-Converters (ADC's). The ADC's had a time lag of 2 μs with respect to the start of the strobe signal 14 μs wide. The bipolar outputs were used for timing and identification purposes. The amplified outputs from the two solid state detectors were fed into the Timing Single Channel Analysers (TSCA's). The three unipolar outputs were brought into coincidence with each other by the delay amplifiers. One of the two bipolar signals which were fed into the OR logic gate generated the strobe signal. The remaining logic signal was processed by the pattern gate in coincidence with a channel zero signal that was a non Δ*E*-*E* event.

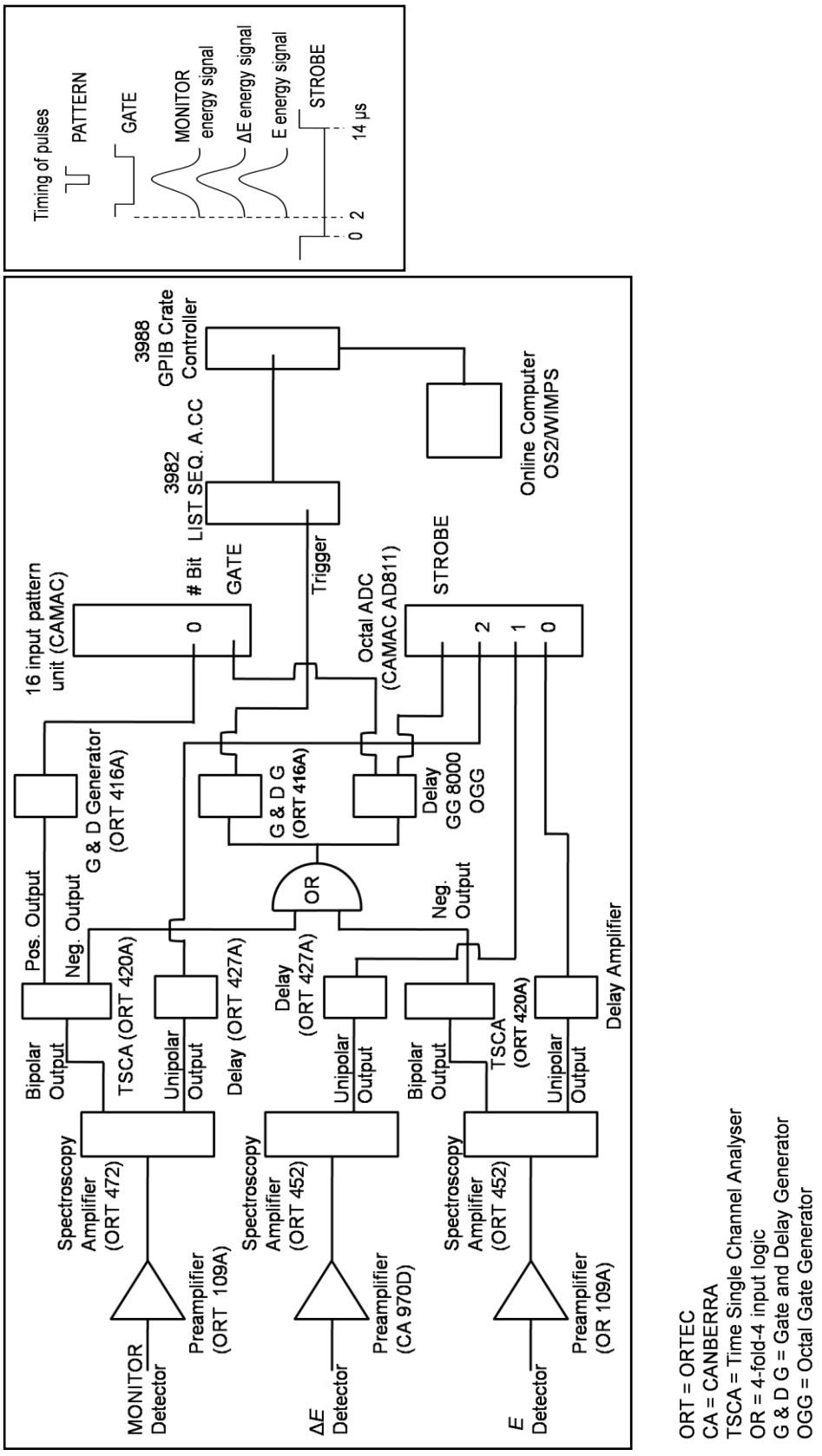


Figure 3.12 Electronics block diagram showing the components used in detected signal processing.

The gate, monitor, ΔE and E signals were brought into time coincidence for processing by the ADC's of the CAMAC data acquisition system. An on-line computer, using OS/2 operating system and WIMPS software [FE92] was used for data extraction and analysis. Plots of ΔE *versus* E_{Total} for each scattering angle were obtained, with $E_{\text{Total}} = E_{\text{Stop}} + n\Delta E$ being the total kinetic energy, where n is a normalisation factor which normalized the ΔE to the E_{Stop} signal and was obtained by comparing the corresponding E_{Stop} signals for the GAS OFF and GAS ON conditions (n = 0.3865). In angular distribution measurements, a monitor detector fixed relative to the target and to the beam direction was used to normalise the individual measurements, being more reliable than a beam current integrator which is sensitive to fluctuations in average charge state of the beam and secondary electron emission from the last Faraday cup on the beam line [WA04]. The monitor detector was used to check on the state of the SiO_2 target.

3.4.3 Data extraction

The 2-dimensional ΔE-E spectra obtained through the use of the gas-ionisation detector were displayed on a computer, for each scattering angle. The upper part of Fig. 3.13 shows a typical 2-dimensional spectrum measured for 30 MeV $^{16}O^{5+}$ ions on a 50 μgcm^{-2} SiO_2 target, at θ_{Lab} = 23°. After projection onto the x-axis using a polygon gate to define the ^{16}O events in the ΔE-E plot, the resulting 1-dimensional spectrum is shown in the lower part of Fig. 3.13. The resolution inherent in the ΔE-E gas-ionisation detector and the Tandem accelerator beam made it possible to resolve the groups of ^{16}O ions elastically scattered from the various target components. The ^{16}O off ^{16}O elastic scattering peaks for each scattering angle were fitted using a Gaussian curve fitting procedure. The following formula was employed:

$$y(x) = h \exp\left\{ -\frac{1}{2}\left(\frac{x - x_0}{\sigma} \right)^2 \right\} + B \,, \tag{3.12}$$

where h is the peak height, x is the channel number, x_0 is the peak centroid, σ is

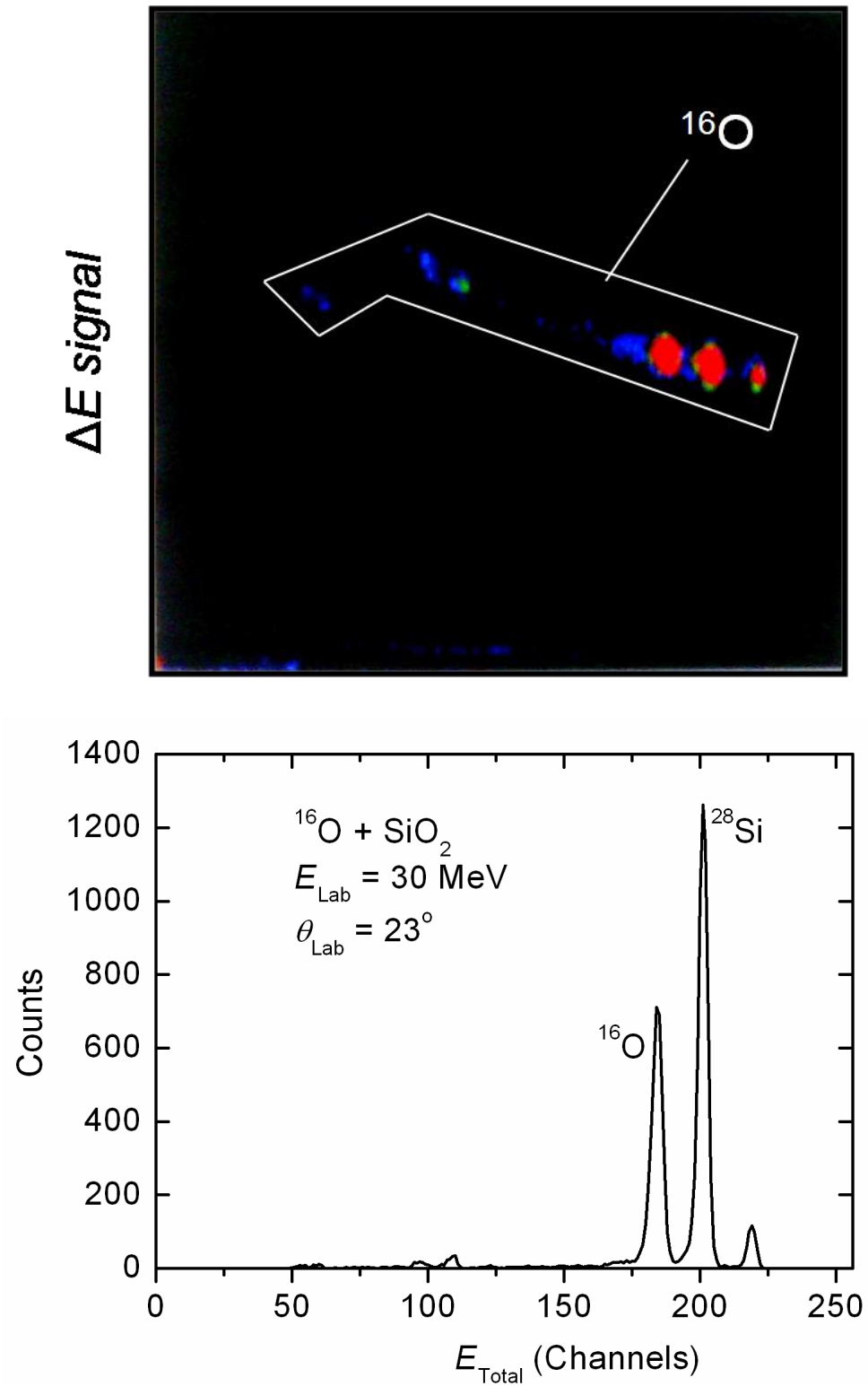


Figure 3.13 *Upper*: Two-dimentional ΔE *versus* E_{Total} spectrum of $^{16}O + SiO_2$. *Lower*: Projected one-dimensional spectrum at $E_{\text{Lab}} = 30$ MeV and $\theta_{\text{Lab}} = 23°$.

the standard deviation and B is the quadratic background defined as

$$B = a_0 + a_1 x + a_2 x^2 . \tag{3.13}$$

The area A_G under a given Gaussian fit was obtained from

$$A_G = h\sigma\sqrt{2\pi} . \tag{3.14}$$

Thus, the total area A_P under a given peak is the sum of the Gaussian fit plus background

$$A_P = A_G + B . \tag{3.15}$$

An estimate of the uncertainty $\pm\Delta A_G$ of the extracted peak area was obtained from

$$\Delta A_G = \sqrt{A_P + B} = \sqrt{(A_G + B) + B} \tag{3.16}$$

which, for small background reduces to the usual statistical error

$$\Delta A_G = \sqrt{A_G} . \tag{3.17}$$

3.4.4 Determination of scattering cross-sections

Experimentally measured elastic scattering cross-sections were obtained as follows:

1. The elastic scattering yield, in the laboratory (Lab) reference frame, was obtained from the Gaussian curve fitting procedure described in Section 3.4.3, for each scattering angle.

2. The monitor detector yield was obtained as for each elastic scattering angle measured.

3. The monitor detector yields were normalised to the start of the measurements at $\theta_{Lab} = 20°$.

4. The normalised Lab yield was obtained by multiplying the normalised monitor yield by the Lab yield for each scattering angle measured. This

procedure is more accurate than using standard beam current integration techniques because of possible variations in the average charge state of the beam.

5. The normalised centre-of-mass (c.m.) yield was obtained, for each elastic scattering angle by multiplying the normalised Lab yield by the respective Lab-c.m. factors, obtained from two body kinematics [MA68]

$$I(\theta_{\text{c.m.}}) = I(\theta_{\text{Lab}})\left(\frac{\sin^2\theta_{\text{Lab}}}{\sin^2\theta_{\text{c.m.}}}\right)\cos(\theta_{\text{c.m.}} - \theta_{\text{Lab}}), \tag{3.18}$$

where $I(\theta_{\text{c.m.}})$ is the intensity (yield) at each scattering angle $\theta_{\text{c.m.}}$ in the centre-of-mass reference frame, $I(\theta_{\text{Lab}})$ is the intensity (yield) at each scattering angle θ_{Lab} in the laboratory reference frame.

6. The ratios to Mott scattering cross-sections (Eq. (2.34)) were obtained for each scattering angle. Table A2 in the Appendix section shows the numerical values obtained. The upper part of Fig. 3.14 shows a plot of the experimental reaction cross-section ratio to Mott as a function of c.m. angle.

7. Finally, all c.m. yields for each elastic scattering angle were normalised to the Mott scattering cross-sections at the smallest scattering angles. The lower part of Fig. 3.14 shows a plot of the absolute cross-sections as a function of c.m. angles.

8. As the main error in these measurements was due to the counting statistics, the final (absolute) error in the normalised c.m. yield was obtained from the percentage errors found from the Gaussian curve fitting procedure of step (1) above. Section 3.4.3 explains how errors were calculated.

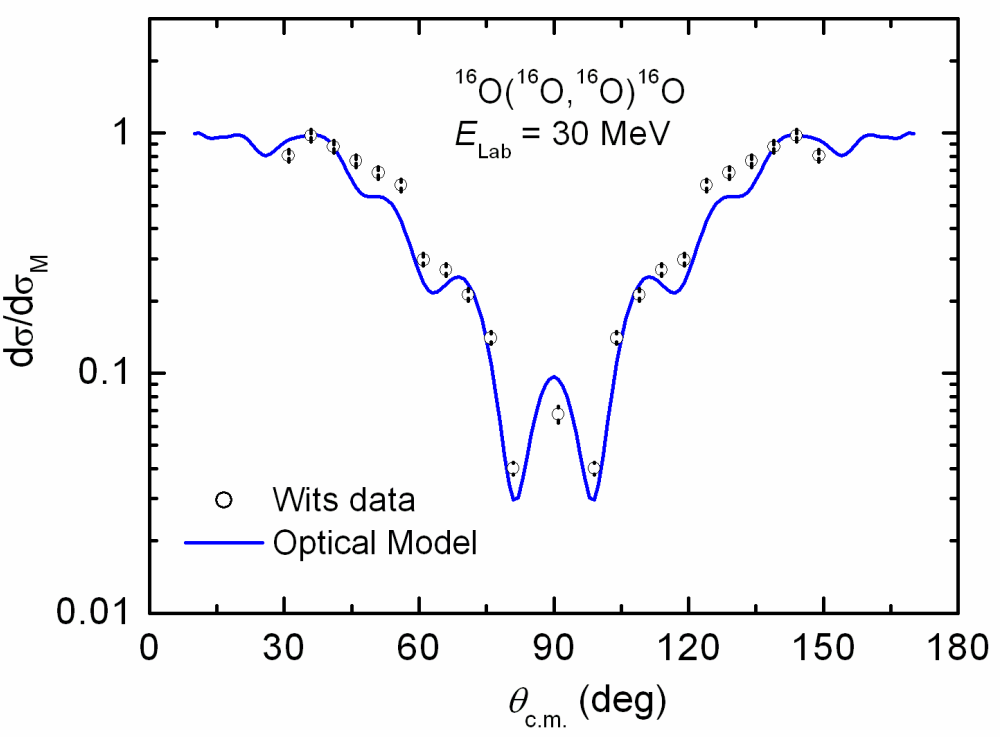
3.4.5 Optical model prediction for $^{16}O + ^{16}O$ elastic scattering

In this section the normalised Wits data for the elastic scattering of $^{16}O + ^{16}O$ are analysed and presented. Calculations for the Mott scattering for the identical ^{16}O and ^{16}O scattering partners together with an optical model calculation for elastic scattering are shown graphically and discussed in detail.

An elastic scattering angular distribution for $^{16}O + ^{16}O$ was measured at E_{Lab} ($^{16}O^{5+}$) = 30 MeV ($E_{c.m.}$ = 15 MeV). This was the maximum achievable incident energy corresponding to the most stable setting of about 5 MV accelerator terminal voltage of the recently refurbrished 6 MV EN tandem at the time of the experiment. The Coulomb barrier for this elastic scattering reaction, in the laboratory reference frame is $E_{Lab}^{CB} = 26.12$ MeV corresponding to a centre-of-mass value of $E_{c.m.}^{CB} = 13.06$ MeV. The angular distribution range was measured in steps of $\theta_{Lab} = 2.5°$ (see Tables 3.2 and A2).

The optical model for elastic scattering used for the present analysis has been described in general terms in Section 2.4, and it makes use of a modified version of the A-THREE computer code [AU78]. In this, the non-relativistic Schrödinger equation, with a complex scattering potential, is solved numerically, partial wave by partial wave, in order to obtain the nuclear phase shifts, from which the elastic scattering cross-sections are calculated. The real part of the optical potential was of a phenomenological Woods-Saxon form and the imaginary part was taken to be one of the volume absorption.

Table 3.4 shows the Woods-Saxon potential parameters used in the optical model fit to the elastic scattering of $^{16}O(^{16}O,^{16}O)^{16}O$. The optical model parameters used in the present study were taken from [CA81, BR61] so as to have a clear comparison with already existing literature data.



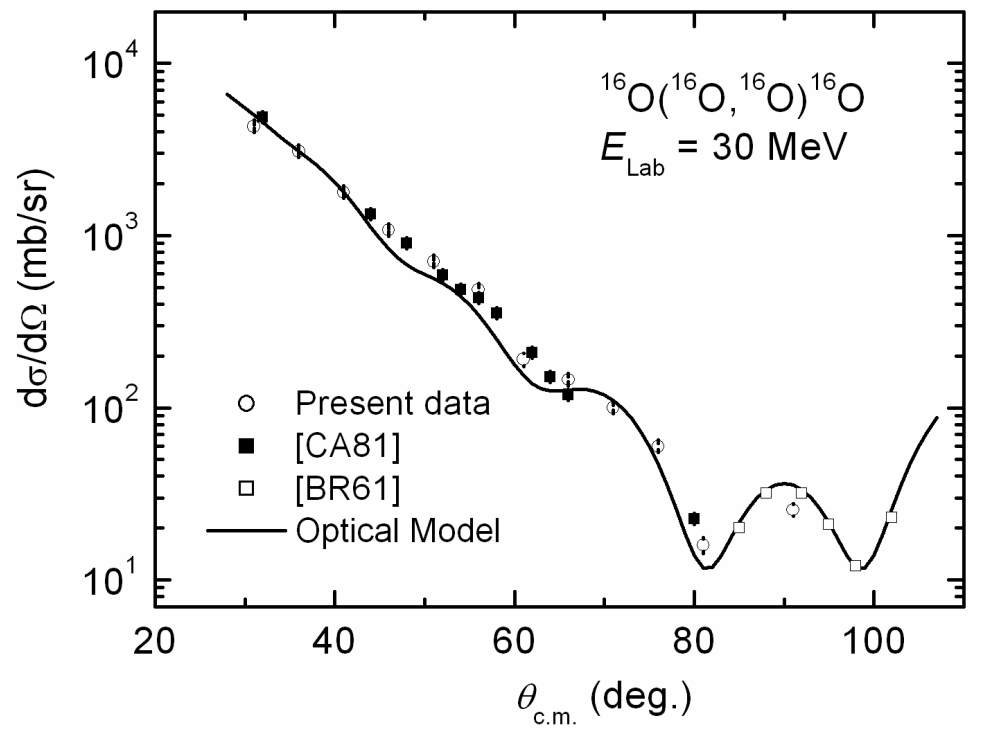


Figure 3.14 Angular distribution for the elastic scattering of ^{16}O from ^{16}O at E_{Lab} = 30 MeV. The solid curves show *Upper*: the symmetrised ratio-to-Mott optical model calculations using the parameters shown in Table 3.4. *Lower*: symmetrised optical model prediction.

Table 3.4 Optical model potential parameters [CA81] for $^{16}O(^{16}O,^{16}O)^{16}O$.

E_{Lab} (MeV)	$E_{c.m.}$ (MeV)	V_0 (MeV)	W_0 (MeV)	R_{0R} (fm)	R_{0I} (fm)	a_R (fm)	a_I (fm)
30	15	17.1	$0.4 + 0.1E_{c.m.}$	1.35	1.35	0.49	0.49

3.4.6 Discussion

The upper part of Fig. 3.14 shows an angular distribution for the elastic scattering of ^{16}O from ^{16}O at E_{Lab} = 30 MeV, where the solid curve shows the symmetrised ratio-to-Mott optical model calculations using the parameters shown in Table 3.4. The measured angular range is between $31° \leq \theta_{c.m.} \leq 91°$ and it was performed in steps of $\theta_{c.m.} = 5°$. The angular distribution exhibits symmetry about 90°, hence, the same experimental values of $d\sigma/d\sigma_{Mott}$ were replotted as shown in the same figure, at corresponding angles above 90°. One can see that the measured data agree well with the optical model prediction. It should be noted by the fact that the chosen incident energy was above the Coulomb barrier and, therefore, nuclear effects come into play.

Further, absolute cross-sections are compared with an optical model prediction as shown in the lower part of Fig. 3.14. Present angular distribution data exhibit a good corespondence with data taken at the same energy [CA81, BR61], which are plotted together with present data for comparison. The optical model theoretical calculation reproduces reasonably well the measured data over the whole angular range as expected [CA81]. In particular, the agreement in shape between the calculated and measured angular distribution is rather striking. This strongly affirms the calibration methods and set-up of the tandem accelerator after its refurbishment. From previous research on analysis of number of angular distributions in excitation functions by Bromley *et al*. [BR61], it has been

established that the real potential extensive parameter variation within the optical model was not successful in reproducing a number of excitation functions in different angles at various energies. While the real potential of V = 17 MeV is constant in energy, this does not seem to be the case with the imaginary potential W, which has been found by the above-mentioned authors to have an energy dependence given by

$$W = 0.4 + 0.1E_{\text{c.m.}}. \tag{3.28}$$

The rather small value, shallowness, of the imaginary potential W somehow implies a long mean free path λ of the interpenetrating ions, given by [BR61]

$$\lambda = \frac{4.6}{-W}\left(\frac{E-V}{\mu}\right)^{1/2}, \tag{3.29}$$

where W is the imaginary potential, E is the centre-of-mass incident energy, V is the real potential and μ is the reduced mass. λ = 4.85 fm at $E_{\text{c.m.}}$ = 15 MeV and 3.27 fm at $E_{\text{c.m.}}$ = 30 MeV. The exact physical significance of this long mean free path remains open to question.

CHAPTER 4

Conclusions

The newly refurbished 6 MV EN tandem accelerator of iThemba LABS (Gauteng) has been calibrated, using the two independent nuclear reactions ^{27}Al(p,n)^{27}Si and ^{12}C(^{16}O,α)^{24}Mg. The analyser magnet calibration constants determined from the two methods agree very well, within error bars. Combining results of the two calibration methods gave a final analyser magnet constant of K = 11.7451 ± 0.0377 keV.u/MHz^2.

The accelerator settings have been adjusted and set using the final value for the analyser magnet constant, leading to a successful ^{16}O(^{16}O,^{16}O)^{16}O elastic scattering angular distribution measurement at E_{Lab} (^{16}O) = 30 MeV. The new scattering data are consistent with the previously measured values in Refs. [BR61, CA81]. The optical model theoretical calculation reproduces reasonably well the measured data over the whole angular range as expected [CA81].

It may thus be concluded that with the successful accomplishment of the above tasks the newly refurbished EN tandem accelerator of iThemba LABS (Gauteng), the Nuclear Physics beam line (C-line) and the ΔE-E gas-ionisation chamber with its associated electronics and data acquisition system have been commissioned and are ready for use in further nuclear structure studies.

For the ^{12}C(^{16}O,α)^{24}Mg* reaction, another optical line up of the C-line is required and more precise determination of scattering angle using subsequent left/right Rutherford scattering.

Bibliography

[AU78] E. H. Auerbach, *A-THREE: A general optical model code especially suited to heavy-ion calculations*, Computer Physics Communications 15 (1978) 165-192.

[AN07] E. Andrade, C. Solis and M. F. Rocha, *Application of the SIMNRA code to calibrate the analyzing magne associated with a Van de Graaff accelerator*, Nuclear Instruments and Methods in Physics Reseach B 261 (2007) 553-556.

[BA67] N. C. Barford, *Experimental measurements: Precision, Error and Truth*, (Addison-Wesley Publishing Company, London, 1967) 63-64.

[BE76] E. M. Bernstein, *Geometry effects in precise threshold determinations*, Phys. Rev. C15 (1976) 1592-1594.

[BR61] D. A. Bromley, J. A. Kuehner and E. Almqvist, *Elastic Scattering of Identical Spin-Zero nuclei*, Phys. Rev. 123 (1961) 878-893.

[CA81] B. O. Carragher, *α-transfer reactions*, MSc Dissertation, University of the Witwatersrand, Johannesburg, 1981.

[EN90] P. M. Endt and C. Van Der Leun, Nuclear Physics A521 (1990) 129.

[FE92] R. W. Fearick, WIMPS computer programme, 1992.

[FR65] J. M. Freeman, J. H. Montague, G. Murray and R. E. White, *The accurate determination of some (p,n) thresholds in the proton energy range 5 to 10 MeV*, Nuclear Physics 65 (1965) 113-129.

[GI95] D. C. Giancoli. *Physics: Principles with Applications*, (Prentice hall, Englewood Cliffs, New Jersey 07652, 4th Edition, 1995) 903- 904.

[IT08] iThemba LABS Annual Report 2008, *Accelerator Group* (2008) 24-25.

[JA70] D. F. Jackson, *Nuclear Reactions*, (Methuen & Co Ltd, London, 1970) 110-137.

[JI08] M. Jingo, C. O. Kureba, J. Carter and E. Sideras-Haddad, *Nuclear structure studies at the 6 MV EN Tandem Accelerator of iThemba LABS (Gauteng)*, 53rd SAIP Annual Conference poster (2008).

[JI09] M. Jingo, C. O. Kureba, J. Carter and E. Sideras-Haddad, *Characteristics and use of a high resolution ΔE-E gas-ionisation detector for nuclear particle identification*, 54th SAIP Annual Conference poster (2009).

[KU09] C. O. Kureba, M. Jingo, J. Carter and E. Sideras-Haddad, *Energy calibration of the 6 MV EN Tandem Accelerator of iThemba LABS (Gauteng)*, 54th SAIP Annual Conference poster (2009).

[KR88] Kenneth S. Krane, *Introductory Nuclear Physics*, (John Wiley & Sons, New York, 1988) 378-440.

[LE78] C. M. Lederer and V. S. Shirley, Table of isotopes, Seventh Edition, (John Wiley, New York, 1978).

[LE87] W. R. Leo, *Techniques for Nuclear and Particle Physics Experiments, A How-to Approach* (Springer-Verlag Berlin Heidelberg, 1987) 24-25.

[MA69] J. V. Maher, M. W. Sachs, R. H. Siemssen, A. Weidinger and D. A. Bromley, Nuclear Interaction of Oxygen with Oxygen, Phys. Rev. 188 (1969) 1665-1682.

[MA66] J. B. Marion, *Accelerator Calibration Energies*, Reviews of Modern Physics 38 (1966) 660-668.

[MA68] J. B. Marion and F. C. Young, *Nuclear Reaction Analysis* (North-Holland-Amsterdam, 1968) 39-41, 140-142.

[MI89] R. Middleton, *Negative ion cookbook*, October 1989.

[MO30] N. F. Mott, Proc. R. Soc. 126 (1930) 259.

[NA77] H. Naylor and R. E White, *An accurate measurement of the $^{27}Al(p,n)^{27}Si$ threshold energy*, Nuclear Instruments and Methods 144 (1977) 331-335.

[OL87] D. K. Olsen, K. A. Erb, C. M. Jones, W. T. Milner, D. C. Weisser and N. F. Ziegler, Nucl. Instr. and Meth. in Phys. Res. A254 (1987) 1-6.

[OV69] J. C. Overley, P. D. Parker and D.A. Bromley, Nucl. Instr. and Meth. 68 (1969) 61-69.

[PU77] F. Puhlhofer, *On the interpretation of evaporation residue mass distributions in heavy-ion induced fusion reactions*, Nucl. Phys. A280 (1977) 267-284.

[RI66] G. Rickards, B. E. Bonner and G. C. Phillips, *Measurement of (p,n) thresholds at tandem energies*, Nuclear Physics 86 (1966) 167-186.

[SI90] A. G. Sitenko, *Theory of Nuclear Reactions* (World Scientific, Singapore, 1990) 186.

[WA85] A. H. Wapstra and G. Audi, *The 1983 Atomic Mass Evaluation (I). Atomic Mass Table*, Nucl. Phys. A432 (1985) no. 1

[WA04] R. L. Wabwile, *Inelastic excitation of unbound states in bosonic (^{6}Li + ^{6}Li) and fermionic (^{9}Be + ^{9}Be) heavy-ion systems*, MSc research report, University of the Witwatersrand, (2004).

[TH91] Thermo Electron Corp. RM&P, *Neutron Rem Detector Technical Manual*, (January 1991).

[TH92] Thermo Electron Corp, *Eberline Smart Portable Technical Manual*, (February 1992).

Appendix

TABULATED VALUES OF THE MEASURED QUANTITIES

TABLE A1: $^{27}Al(p,n)^{27}Si$ analyser magnet calibration measured data.

NMR frequency (MHz)	Neutron yield (counts x 10^{-3} nC^{-1})	Error (%)	(Yield - Background)$^{2/3}$	Error (%)
22.21541	144.46	2.13	-	-
22.26370	148.11	2.01	-	-
22.31190	153.55	2.04	-	-
22.36024	161.78	1.90	5.52	1.25
22.38776	160.85	1.94	5.25	1.66
22.41404	175.84	1.86	9.01	1.45
22.45033	186.86	1.80	11.31	1.30
22.46348	182.62	1.87	10.46	1.83
22.47588	184.79	1.90	10.90	2.38
22.48765	188.04	1.83	11.55	1.53
22.49993	192.60	1.84	12.42	1.80
22.53438	197.10	1.74	13.26	1.15
22.56080	205.77	1.73	14.80	1.27
22.58380	208.29	1.64	15.24	0.93
22.61236	232.01	1.62	19.06	1.10
22.62763	237.52	1.60	19.89	1.07
22.63808	258.55	1.52	22.92	1.01
22.65593	272.03	1.48	24.76	0.97
22.69332	295.55	1.41	27.82	0.92
22.72709	342.04	1.32	33.42	0.91
22.75790	376.14	1.24	37.25	0.86

TABLE A2: Identical particle $^{16}O(^{16}O,^{16}O)^{16}O$ elastic scattering measured data at E_{Lab} = 30 MeV.

θ_{Lab} (deg.)	$\theta_{c.m.}$ (deg.)	$d\sigma/d\sigma_M$	Error	$d\sigma/d\Omega$ (mb/sr)	Error (mb/sr)
15.5	31.00	803.46E-3	19.60E-3	4310.16	105.17
18.0	36.00	976.52E-3	19.73E-3	3088.13	62.38
20.5	41.00	876.76E-3	16.57E-3	1786.47	33.76
23.0	46.00	764.42E-3	14.68E-3	1077.66	20.69
25.5	51.00	683.59E-3	17.50E-3	707.41	18.11
28.0	56.00	606.60E-3	18.8E-3	484.72	15.03
30.5	61.00	296.15E-3	9.63E-3	191.04	16.64
33.0	66.00	268.94E-3	8.82E-3	145.75	4.78
35.0	71.00	211.93E-3	6.97E-3	100.09	3.29
38.0	76.00	140.03E-3	5.59E-3	59.63	2.38
40.5	81.00	40.08E-3	2.08E-3	15.90	1.69
45.5	91.00	67.44E-3	5.27E-3	25.47	1.99